Fractional Focusing and the Chirp Scaling Algorithm

With Real Synthetic Aperture Radar Data

by

Judith A. Northrop

A Thesis Presented in Partial Fulfillment
of the Requirements for the Degree
Master of Science

Approved April 2011 by the
Graduate Supervisory Committee:

Antonia Papandreou-Suppappola, Chair
Andreas Spanias
Cihan Tepedelenlioglu

ARIZONA STATE UNIVERSITY

May 2011

ABSTRACT

For synthetic aperture radar (SAR) image formation processing, the chirp scaling algorithm (CSA) has gained considerable attention mainly because of its excellent target focusing ability, optimized processing steps, and ease of implementation. In particular, unlike the range Doppler and range migration algorithms, the CSA is easy to implement since it does not require interpolation, and it can be used on both stripmap and spotlight SAR systems. Another transform that can be used to enhance the processing of SAR image formation is the fractional Fourier transform (FRFT). This transform has been recently introduced to the signal processing community, and it has shown many promising applications in the realm of SAR signal processing, specifically because of its close association to the Wigner distribution and ambiguity function.

The objective of this work is to improve the application of the FRFT in order to enhance the implementation of the CSA for SAR processing. This will be achieved by processing real phase-history data from the RADARSAT-1 satellite, a multi-mode SAR platform operating in the C-band, providing imagery with resolution between 8 and 100 meters at incidence angles of 10 through 59 degrees. The phase-history data will be processed into imagery using the conventional chirp scaling algorithm. The results will then be compared using a new implementation of the CSA based on the use of the FRFT, combined with traditional SAR focusing techniques, to enhance the algorithm's focusing ability, thereby increasing the peak-to-sidelobe ratio of the focused targets. The FRFT can also be used to provide focusing enhancements at extended ranges.

To my family, friends and colleagues,

I could not have completed this degree

without your never ending support.

ACKNOWLEDGEMENTS

Without hesitation, I sincerely want to express my deep gratitude to Professor Antonia Papandreou-Suppappola for encouraging my studies and research. This thesis would not be possible without her detailed analysis, recommendations and efforts on my behalf. She has also remained my strongest advocate in representing my needs to the ASU Graduate College. Professor Papandreou-Suppappola's enthusiasm in the field of signal processing and devotion to teaching and her students has truly been inspiring.

I would also like to thank Professors Andreas Spanias and Cihan Tepedelenlioglu for their interest in my research, and agreeing to serve as members of my supervisory committee.

A very special thank you to Cynthia Cantrell, for her patience and constant encouragement while supporting me through school, jobs, relocation and all of my endeavours no matter how trying.

Heartfelt thanks are due to Toni Pardi for her friendship and constant encouragement throughout the past year, not only for support while implementing the fractional Fourier transform, but for her detailed editorial guidance.

I must thank my proof readers, Janette Cantrell, Forest Brown and Ken Ward for having interest in my research and being willing to lend a hand.

I must recognize Jim Sagmiller at Northrop Grumman for initially inspiring me to study SAR signal processing, and my former colleagues at Lockheed Martin in Goodyear, Arizona, for countless hours in collaboration studying radar processing concepts.

Finally, a special thank you to Ian Cumming and Frank Wong for writing *digital processing of Synthetic Aperture Radar Data*; and Walter Carrara, Ron Goodman, and Ronald Majewski for writing *Spotlight Synthetic Aperture Radar: Signal Processing Algorithms*. These two textbooks have provided me with countless hours of study and invaluable reference for my interest in SAR signal processing.

TABLE OF CONTENTS

CHAPTER Page

CHAPTER Page

LIST OF FIGURES

LIST OF TABLES

CHAPTER 1

Introduction

1.1 Research, Motivation and Objectives

Synthetic aperture radar (SAR) is a microwave imaging technique capable of providing high-resolution imagery from data collected by a relatively small antenna [4]. The SAR takes advantage of the forward motion of the platform while transmitting and receiving short waveforms or pulses to form the equivalent of a long antenna. It is a coherent system, in that it retains both the phase and magnitude of the received echos which are synthesized in the signal processor to produce high resolution imagery [5]. Compared to passive electro-optical systems, SAR is an active system capable of collecting imagery in day/night and cloud cover conditions.

SAR was initially developed by Carl Wiley at Goodyear Aircraft Company in Goodyear, Arizona, in 1951 and was originally called Doppler Radar Beam Sharpening. With the onset of Moore's law and the digital processor, this technology has continued to evolve from the early optical processors, where phase-history was recorded on film and processed on an optical bench, to today's high speed digital processors. For strip-mapping SAR, where the antenna is fixed with respect to the platform, high resolution radar images are formed on digital processors using two-dimensional (2-D) correlation algorithms. For spotlight SAR, where the antenna is steered to continuously illuminate the same spot, image formation relies on the principle of computer tomography [4]. Another imaging mode is inverse synthetic aperture radar (ISAR), where the antenna or radar beam is stationary and the movement of the target is used to create the synthetic aperture. Based on the imaging modes, different image formation algorithms are used. Strip-mapping SAR uses range Doppler, range migration and chirp scaling algorithms for image formation [1], whereas spotlight SAR uses the polar format, range migration and chirp scaling al-

gorithms [6]. The image formation methods used by ISAR combine the range Doppler algorithm (RDA) along with time-frequency methods such as linear frequency-modulated (LFM) chirp detection approaches [7, 8]. Note that SAR signals containing moving targets (including ISAR) are multi-component LFM signals and, in order to separate and focus this energy, efficient LFM detection methods are necessary [8].

For high quality imagery, autofocus methods are necessary to remove quadratic and higher order phase errors caused by uncompensated motion between the antenna and the scene being imaged. Other phase error sources are algorithm/hardware limitations and propagation effects [6]. To correct for these phase errors (which can cause image defocus), autofocusing techniques are used to estimate the phase error and correct it using a phase cancellation filter. As with the image formation algorithms, different autofocus methods are more applicable to the imaging modes. For strip-mapping, map-drift and contrast maximization methods are used [1], and for spotlight, phase gradient autofocus (PGA), map-drift and contrast maximization methods are commonly used [6, 9].

The chirp scaling algorithm (CSA) for SAR image formation was first introduced in 1994 [10] and has had wide spread acceptance, mainly due to its good focusing capabilities and ease of implementation. The CSA provided a means of performing range cell migration correction (RCMC) using fast Fourier transform (FFT) complex multiplication methods. This approach is inherently phase preserving and can be implemented more efficiently than the interpolation method used by the conventional RDA, where accuracy is limited to the size of the interpolation kernel and depends on range varying coefficients [1, 6]. Another feature of the CSA is that it provides secondary range compression (SRC) in its 2-D match filtering process. The SRC is an efficient method for handling the range-azimuth coupling, which becomes increasingly necessary for large-swath, large-beamwidth and high squint angle applications.

Recently, the fractional Fourier transform (FRFT) has been used to enhance the fo-

cusing capabilities of the CSA [2]. The FRFT is a subset of the Fourier transform (FT) that was introduced in the field of optics by Namias in the 1980s [11] and then to the signal processing community in 1994 [2, 12]. Whereas the FT forms orthogonal coordinates used to define the time-frequency (TF) plane, the FRFT generalizes the FT by providing a continuum of fractional domains between the conventional TF domain [13]. The FRFT achieves this by rotating the TF plane in the counter clockwise direction with the use of a rotational parameter α, which is periodic with period 2π. Since the FRFT is a generalization of the FT, it is also a linear, unitary transform.

Having unitary and Hermitian operators associated with the FRFT [14, 15] allows for a definition of the fractional autocorrelation function [13]. The fractional autocorrelation function at arbitrary angles corresponds to radial slices of the ambiguity function (AF) passing through the origin at the same arbitrary angles, reducing a 2-D AF search to a 1-D fractional autocorrelation function search [16, 17]. Using a fast discrete FRFT approximation with the fractional autocorrelation function provides an efficient detection method, especially for LFM signals, in low signal-to-noise ratio (SNR) environments. To characterize the accuracy of LFM detection using the FRFT in varying SNR environments, the Cramér-Rao lower bound (CRLB) for LFM mean squared error is often used as a threshold for comparing the fractional autocorrelation function results.

The integration of the CSA with the FRFT is called the *fractional chirp scaling algorithm* (FrCSA) [2]. Specifically, the FRFT enhances the CSA processing using a local optimization procedure (LOP), and the resulting FrCSA provides significant improvements to the SNR and sidelobe reduction ratio (SLRR) when compared to classical FFT implementations.

One measure of SAR image quality is the quadratic phase error (QPE) [1, 6], which, if not corrected, will contribute to elevated sidelobes and a broadening of a target's impulse response width (IRW). A mismatch of frequency-modulation (FM) chirp rates between

the received signal and the matched filter will contribute to QPE, thereby decreasing image quality. One cause for the mismatch is the uncompensated motion between the radar antenna and the target. In addition to using the FRFT to enhance the focusing capabilities of the CSA, recent works have indicated that the FRFT has desirable properties that can be used to develop new methods for correcting this mismatch [2, 8, 18]. To use the FRFT to enhance the CSA, we will leverage the FrCSA concept of using the LOP to produce an optimal response by first detecting the FM chirp rate mismatch using the fractional autocorrelation function. The FM rate mismatch will be corrected in the range direction on a pulse-by-pulse basis in the unprocessed phase-history data prior to CSA processing. Since this occurs prior to image formation, it can be considered an update to the motion compensation to correct for line-of-sight (LOS) translational motion. This update causes changes in the distance between the target and sensor. For corrections in the azimuth direction (QPE caused by estimation error of the effective radar velocity), we will use an LOP to maximize a target's contrast, thereby providing improvements in SNR and peak-to-sidelobe ratio (PLSR). Having the ability to maximize contrast using the FRFT is a result of the extra degree of freedom provided by the use of the transform [2].

1.2 Thesis Organization

The rest of this thesis is organized as follows. Chapter 2 provides the CSA signal model and is the basis for improvements provided by the application of fractional optimization techniques. The signal model is derived in Ian Cumming's and Frank Wong's book, *digital processing of Synthetic Aperture Radar Data* [1]; it is presented in this section and will be cited throughout this thesis. Another book by Walter Carrara, Ron Goodman and Ronald Majewski *Spotlight Synthetic Aperture Radar: Signal Processing Algorithms* [6] provides a derivation of the CSA and is also referenced in this section.

Chapter 3 provides an overview of the fractional Fourier transform by providing the

FRFT kernel and listing some of the key properties, specifically the relationship with the FT and the FRFT additivity property. The relationship of the FRFT with the Wigner distribution, and thus the ambiguity function, is also presented. This relationship is needed to demonstrate how the fractional autocorrelation function is used in LFM detection. The limitation of not having a fast FRFT algorithm comparable to the FFT is noted along with a method for computing the continuous FRFT with complexity $O(N \log_2 N)$, where N is the signal length.

For the FRFT to be a useful tool in SAR signal processing, a transform rotational parameter is necessary to tune the transform for an optimal response. By concentrating on the mismatch between the CSA matched filter FM rates and the FM rates of the returned SAR signal, LFM detection can be used to obtain the FRFT optimal parameters. Chapter 4 examines LFM detection accuracy by comparing the FRFT detection performance with the CRLB for LFM signals.

Chapter 5 presents the proposed focusing technique which is based on enhancing the CSA using the FRFT with optimizations obtained using a local optimization procedure. This fractional focusing method is a first attempt at implementing the FrCSA as provided in [2], with modifications necessitated by using optimized FRFT rotational parameters for a RADARSAT-1 scene.

In Chapter 6, we use a local optimization procedure to detect the FM rate mismatch between the signal and the matched filter using the fractional autocorrelation function. The mismatch in FM rates are used to optimize the FRFT pulse compression response for a RDRASAT-1 scene, by providing the optimizations to the enhanced focusing CSA as provided in Chapter 5. Comparisons of the CSA and enhanced CSA are provided by evaluation of contrast and point target analysis.

CHAPTER 2

Chirp Scaling Algorithm

2.1 Chirp Scaling Algorithm Description

The chirp scaling algorithm (CSA), also known as the differential range deramp algorithm, was presented in [1, 6, 10] as a refinement of the classical range Doppler algorithm (RDA) to provide very high quality synthetic aperture radar (SAR) imagery. The CSA has received widespread acceptance due to its efficient implementation and the ability to perform secondary range compression (SRC), which can limit the focusing accuracy of higher squint and wide-aperture systems using the RDA. This improvement is a benefit of the phase-history data being available in the 2-D frequency domain where SRC can be made azimuth frequency dependent. While the RDA algorithm uses interpolation to implement range cell migration correction (RCMC), the CSA uses (a) frequency shifting to correct for the constant migration component, and (b) chirp scaling to correct for the linear migration component. The net result of the scaling and shifting operations, also referred to as differential and bulk RCMC, respectively, is that a target's energy is aligned to the correct range position.

As the scaling operation is better matched to chirp-encoded signals, a requirement for the CSA is that the signal or phase-history data must be chirped in the range direction. If the collection system employs a de-ramp or de-chirp on receive, as many do, the chirp-encoding will need to be reapplied prior to the scaling operation. Also, the CSA works well for both stripmap and spotlight SAR collection systems [6].

We consider a signal, such as a linear frequency-modulated (LFM) chirp, that is given by

$$s(t) = \exp\left(j2\pi(K_r/2)t^2\right) \tag{2.1}$$

with frequency-modulation (FM) rate K_r Hz^2, that is transmitted by a SAR. The signal is

reflected off a point reference target and is migrated at different azimuth locations η due to constant changes in range throughout the synthetic aperture. The time taken for the signal to travel to the target and return is given by $\tau = 2R/c$, where R is the range of the target from the radar and $c = 3 \times 10^8$ m/s is the speed of wave propagation in light. This scenario is depicted in Figure 2.1. The received baseband signal after the range migration is given by [1],

$$s_r(t,\eta) \;=\; A_0\, w_r\!\left(t - \frac{2R_\eta}{c}\right) w_a\!\left(\eta - \frac{\eta_c}{c}\right) e^{-j4\pi f_0 R_\eta / c}\; s\!\left(t - \frac{2R_\eta}{c}\right), \qquad (2.2)$$

where

$$R_\eta = \left(R_0^2 + V_r^2\,\eta^2\right)^{1/2}, \qquad (2.3)$$

η is the azimuth time, A_0 is an arbitrary complex constant, η_c is the beam center offset time, $w_r(t)$ is the rectangular range envelope function, $w_a(\eta)$ is the sinc-squared azimuth envelope function, f_0 is the radar center frequency, R_η is the slant range at azimuth time η, R_0 is the slant range of closest approach, and V_r is the effective radar velocity.

To correct for this range migration and shift the signal to its proper location, a frequency modulation is applied to a chirp-encoded signal to achieve a shift or scaling of the signal [19]. Note that the maximum shift or scale change that can be implemented by the frequency modulation cannot be too large in order to avoid any problems with the associated change in the signal's center frequency and bandwidth. This restriction is mitigated by applying RCMC in two steps so that only the difference in range cell migration (RCM) at different ranges is corrected in the chirp scaling operation and the bulk RCM is completed in the 2-D frequency domain along with SRC [1]. The η_0 point in Figure 2.1 is also referred to as the broadside range position, which is the position where the azimuth frequency $f_\eta = f_{\eta_c}$. Since the energy of a target should align along a constant range, the range to a target in this pulse will be the range for which the target energy of all pulses are corrected to. In other words, no RCMC will be applied to the pulse corresponding to η_0.

The CSA consists of four fast Fourier transforms (FFTs) and three phase multiplies. Its derivation can be provided using Equation (2.2) for the received baseband signal and the range equation in (2.3). Note that the signal is transformed into the 2-D frequency domain with the use of 1-D FFTs and the principle of stationary phase (POSP) which is used to approximate the Fourier transform (FT) integrals.

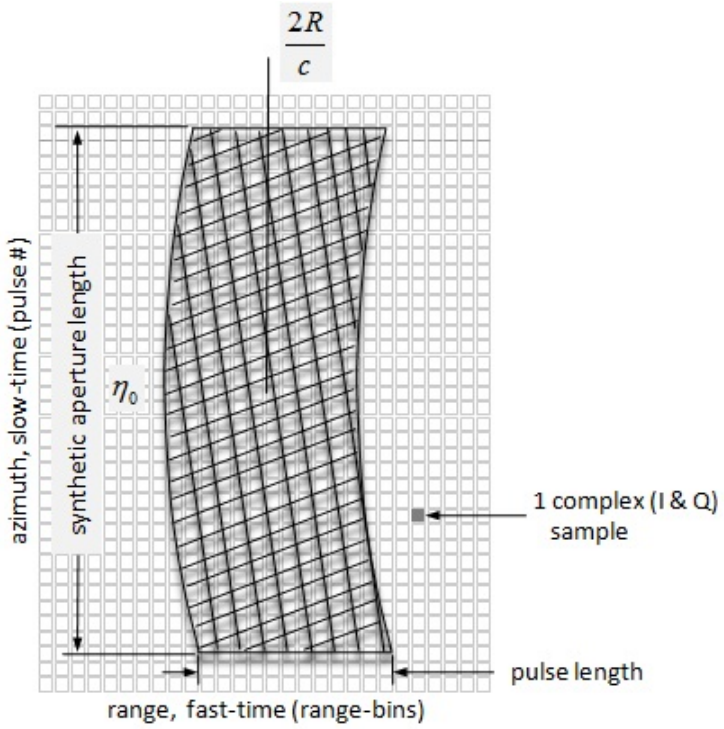

Figure 2.1: Range migration of a single target in 2-D processor memory, with each cell corresponding to an in-phase quadrature or I & Q complex sample format.

The CSA steps are presented in [1], and Figure 2.2 is a flow diagram of the algorithm. Given phase-history data which is in the range-time/azimuth-time domain, the CSA steps are as follows.

1. The azimuth FFT is first computed in order to transform the received data, $s_r(t, \eta)$, into the range Doppler domain.
2. Chirp scaling is applied, using a phase multiply to equalize the range migration of all targets.

3. A range FFT is used to transform the data to the 2-D frequency domain.
4. A phase multiply is performed with a reference function, which applies range compression, SRC, and bulk RCMC in the same operation.
5. A range inverse FFT (IFFT) is performed to transform the data back to the range Doppler domain.
6. A phase multiply is performed to apply azimuth compression with a time varying match filter. A phase correction is also required as a result of the chirp scaling in step 2, which can be incorporated into the same phase multiply.
7. The final azimuth IFFT is computed to transform the compressed data to the SAR image domain.

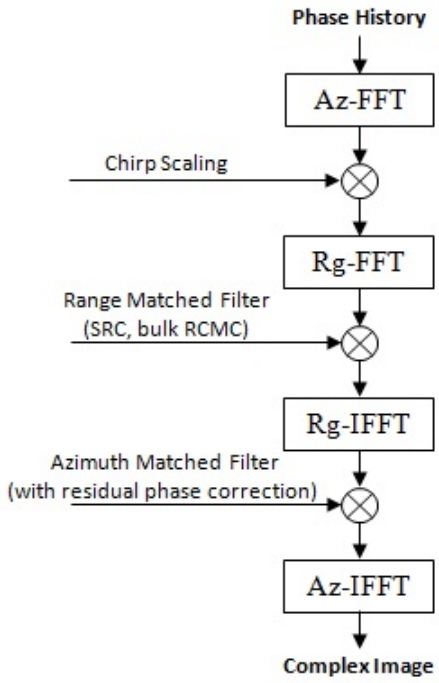

Figure 2.2: Flow diagram of the chirp scaling algorithm. Here, Rg corresponds to range and Az corresponds to azimuth.

Figure 2.3 shows the collection geometry for an orbiting platform. The CSA is similarly applicable to airborne platforms. The slant range variable R is actually the instantaneous slant range R_η that continuously changes as the beam footprint moves across the

target at V_r. As shown in (2.3), a target's slant range will be hyperbolic due to the constant change in range from the broadside position of the antenna.

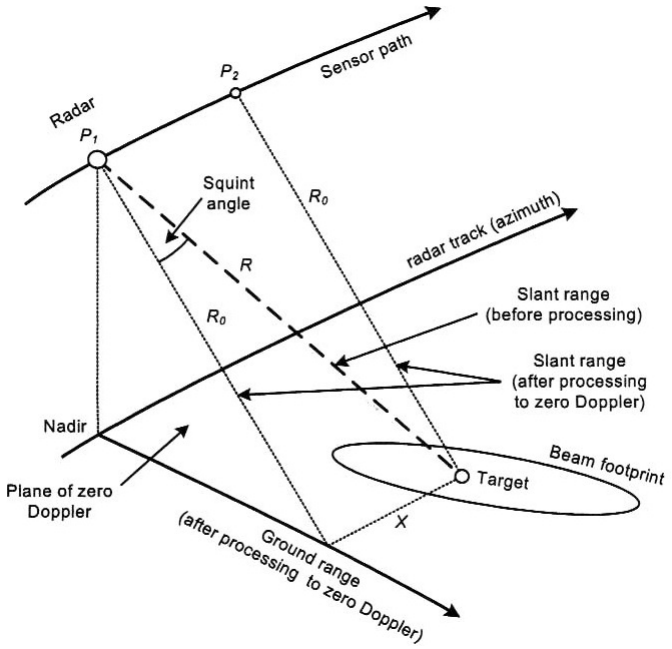

Figure 2.3: Satellite collection geometry, Figure taken from [1].

Figure 2.4 provides a definition of the image data array and demonstrates how the azimuth and range directions are referenced. The conventions in Figures 2.1 and 2.4 will be used throughout this study, in that range will always be increasing from left to right and azimuth will always be increasing from bottom to top. The term fast-time will indicate the range direction and range-bin will be used to indicate a column vector at a constant range. The term slow-time will indicate the azimuth direction and pulse number will indicate a row vector of constant azimuth.

During the imaging operation or collect, pulses are received at the pulse repetition frequency (PRF) and sampled at the range sampling rate to form the 2-D data array suitable for image formation processing. In Figure 2.4, the variables ρ_r and ρ_a refer to the range and azimuth resolutions, respectively. For a radar signal, range is the linear distance along the line of sight from the radar to target. For stripmap systems with relatively

small squint, range is approximately perpendicular to the radar flight path and its resolution is given with $\rho_r = c/(2\text{BW})$, where c is the speed of wave propagation in light and BW is the transmitted bandwidth. For two objects to be resolved,in the range direction, they must be separated by a distance greater than the resolution ρ_r. Azimuth is the linear distance in the direction parallel to the radar flight path. It can also be considered as the along-track direction in an image, since it is the relative along-track position of an object within the antenna's field-of-view, following the radar's line of flight. For stripmap systems with relatively small squint, the azimuth direction is perpendicular to the range direction, and the resolution of an image in the azimuth direction is normally quoted as $\rho_a = L_a/2$, where L_a is the length of the antenna along the azimuth direction. For two objects to be resolved,in the azimuth direction, they must be separated by a distance greater than the resolution ρ_a.

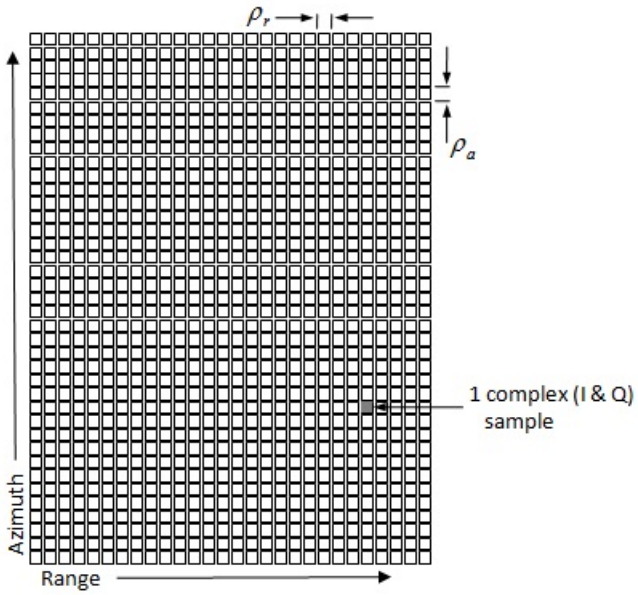

Figure 2.4: Range and azimuth reference to image data array. Each cell (corresponding to an in-phase quadrature or I & Q complex sample format) represents the range resolution ρ_r and azimuth resolution ρ_a.

2.2 Example of Chirp Scaling

As noted, the chirp scaling concept was initially explained in [19] and the example discussed in this section for SAR range processing was provided in [1]. Since the term scaling is customarily used to indicate time or axis scaling, we wanted to provide this example to clarify its use in the CSA and also show how the residual phase term is a product of the scaling operation. In particular, by chirp scaling, we only mean multiplying an LFM chirp by an exponential linear phase term to cause a frequency shift in the LFM chirp; then we show that this is equivalent to a time shift of the LFM chirp.

2.2.1 Constant Shift (bulk RCMC)

In order to demonstrate the CSA with a constant shift, we multiply the LFM chirp with chirp rate K_r, and shifted in time $t = t_a$,

$$s_0(t) = \exp\left\{ j2\pi(K_r/2)(t-t_a)^2 \right\} \tag{2.4}$$

with the following complex exponential linear phase signal (also called the scaling function)

$$s_p(t) = \exp\{ j2\pi K_r(t-t_a)\Delta t \} \tag{2.5}$$

to obtain the scaling operation

$$s_1(t) = s_0(t)s_p(t) = \exp\left\{ j\pi(K_r/2)(t-t_a)^2 \right\} \exp\left\{ j2\pi(t-t_a)\Delta t \right\} \tag{2.6}$$

This multiplication actually results in frequency shifting the LFM chirp $s_0(t)$ by $f_{sc} = K_r\Delta t$. This multiplication is also referred to as chirp scaling. By rearranging the terms in Equation (2.6), we can also express it as,

$$s_1(t) = \exp\left\{ j\pi(K_r/2)(t-t_a+\Delta t)^2 \right\} \exp\left\{ -j\pi K_r\Delta t^2 \right\}. \tag{2.7}$$

Equation (2.7) shows that the frequency-shifted (or scaled) LFM chirp by $f_{sc} = K_r \Delta t$ is equivalent to time-shifting the LFM by $t_{sc} = \Delta t$ plus an undesired residual phase that can be removed during azimuth matched filtering [1].

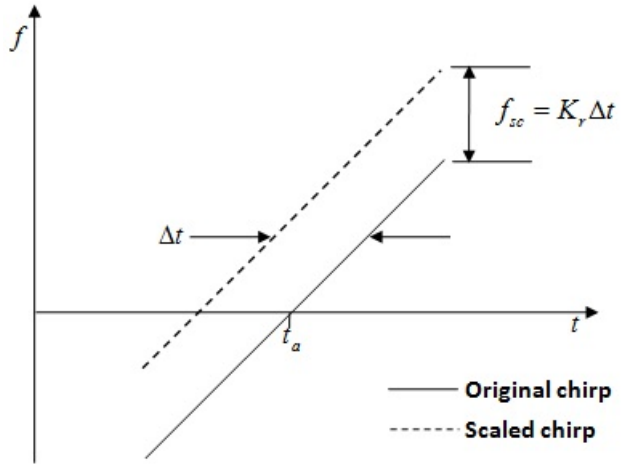

Figure 2.5: Time-frequency chirp scaling (constant shift).

Figure 2.5 is a plot of the time-frequency plane showing how the scaling or frequency shift $f_{sc} = K_r \Delta t$ causes the Δt shift from the original center t. This constant shift in frequency is the bulk RCMC in the CSA.

2.2.2 Shift Varying Linearly with Range (differential RCMC)

Figure 2.6 shows three equally spaced targets in the time-frequency (TF) plane having the same FM rate. The scaling function (dashed line) is itself an LFM signal and for this example, αK_r is positive causing a compression of the range scale. This compression results in the targets shifting closer to the center reference point. In the derivation of the CSA, all targets are shifted in relation to a common reference location in range (R_{ref}) which is a line where no time shift is applied. In Figure 2.6, R_{ref} will correspond to the center target where $t = 0$. For this example, we will use the following LFM scaling

function,

$$s_p(t) = \exp\left\{ j2\pi(\alpha K_r/2)t^2 \right\}. \tag{2.8}$$

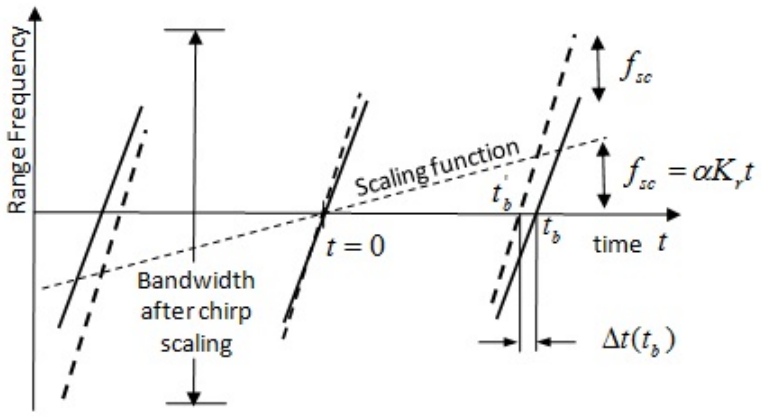

Figure 2.6: Chirp scaling effect on the range position of three targets with the same FM rate.

When we multiply $s_0(t)$ with $t_a = 0$ in (2.4) with the LFM scaling function in (2.8), the resulting scaling transformation is a change in the FM rate of the LFM chirp from K_r to $K_r(1+\alpha)$. Specifically, the new LFM chirp signal is given by,

$$s_{sc}(t) = s_0(t)s_p(t) = \exp(j\pi K_r t^2)\exp(j\pi\alpha K_r t^2) = \exp(j\pi K_r(1+\alpha)t^2) \tag{2.9}$$

which changes the frequency of each target by $f_{sc} = \alpha K_r t$. In other words, the shift in time or range is provided by αt and is proportional to the distance from R_{ref} or $t = 0$. The frequency shift Δf required to move the target from t_b to t_b' can be obtained from,

$$\Delta f t_b = K_r(t_b' - t_b) = -K_r \Delta t_b'. \tag{2.10}$$

This relationship can be shown in the time-frequency plane using the Wigner distribution of the original LFM chirp and the transformed LFM chirp. Specifically, it can be shown that [20]

$$W_{s_{sc}}(t,f) = W_{s_0}(t, f + \alpha K_r t) \tag{2.11}$$

where

$$W_{s_0}(t,f) = \int_{-\infty}^{\infty} s_0\left(t+\frac{\tau}{2}\right) s_0^*\left(t-\frac{\tau}{2}\right) \exp(-j2\pi\tau f) d\tau \tag{2.12}$$

is the Wigner distribution of $s_0(t)$.

2.3 Chirp Scaling

In the azimuth-time, range-time domain, a target's range curvature will depend on both the azimuth and range position. In the azimuth-frequency range-time domain, also referred to as the range Doppler domain, the range curvature will not depend on the target's azimuth location since all target energy will align along a constant range [6]. For this reason, chirp scaling is applied in this domain using a 2-D or azimuth dependent range phase multiplication.

The first step for the CSA is to compute the FT of the received signal into the range Doppler domain. Since a closed form expression for the transform is not available, an approximation will be used by applying the POSP [1, 21]. Specifically we take the FT of $s_r(t,\eta)$ in Equation (2.2) from the azimuth time η to the Doppler f_η to obtain

$$\begin{aligned} S_{rd}(t,f_\eta) =& Aw_r\left(t-\frac{2R_0}{cD(f_{\eta_{ref}},V_{r_{ref}})}\right) W_a(f_\eta - f_{\eta_c}) \exp\left\{-j\frac{4\pi f_0 D(f_\eta,V_r)}{c}\right\} \\ &\times \exp\left\{\frac{j\pi K_m}{c^2}\left[1-\frac{D(f_\eta,V_{r_{ref}})}{D(f_{\eta_{ref}},V_{r_{ref}})}\right]\left[\frac{R_0}{D(f_\eta,V_r)}-\frac{R_{ref}}{D(f_\eta,V_r)}\right]^2\right\} \end{aligned} \tag{2.13}$$

where A is a complex constant, $W_a(f_\eta)$ is the Doppler spectrum envelope or FFT of $w_a(\eta)$ in (2.2), $D(f_\eta,V_r)$ is the migration parameter in the range Doppler domain for the effective radar velocity V_r and is given by,

$$D(f_\eta,V_r) = \sqrt{1-\frac{c^2 f_\eta^2}{4V_r^2 f_0^2}}, \tag{2.14}$$

and K_m is the modified range FM rate

$$K_m = \frac{K_r}{1 - K_r c R_0 f_\eta^2 / (2V_r^2 f_0^3 D^3(f_\eta, V_r))}. \tag{2.15}$$

For LFM chirps, the azimuth dependent scaling function is given by

$$s_{sc}(t, f_\eta) = \exp\left\{ j\pi K_m \left[\frac{D(f_{\eta_{ref}}, V_{r_{ref}})}{D(f_\eta, V_{r_{ref}})} - 1 \right] t^2 \right\} \tag{2.16}$$

assuming no shift was applied to the target at R_{ref}.

With the $S_{rd}(t, f_\eta)$ and $s_{sc}(t, f_\eta)$ defined as in (2.13) and (2.16) respectively, the azimuth dependent chirp scaling is achieved with

$$S_1(t, f_\eta) = s_{sc}(t, f_\eta) S_{rd}(t, f_\eta). \tag{2.17}$$

2.4 Range Compression

After the chirp scaling phase multiplication, the phase-history data is transformed to the azimuth-frequency, range-frequency domain by taking the FT of $S_1(t, f_\eta)$ in the range direction, from t to f_t, to obtain $S_2(f_t, f_\eta)$. The data is now in the 2-D frequency domain and the POSP is used again to evaluate the integral providing $S_2(f_t, f_\eta)$

$$\begin{aligned} S_2(f_t, f_\eta) = {} & A_1 W_r(f_t) W_a(f_\eta - f_{\eta_c}) \\ & \times \exp\left\{ -j \frac{4\pi R_0 f_0 D(f_\eta, V_r)}{c} \right\} \exp\left\{ -j \frac{\pi D(f_\eta, V_r)}{K_m D(f_{\eta_{ref}}, V_r)} f_t^2 \right\} \exp\left\{ -j \frac{4\pi R_0}{c K_m D(f_{\eta_{ref}}, V_{r_{ref}})} f_t \right\} \\ & \times \exp\left\{ -j \frac{4\pi}{c} \left[\frac{1}{D(f_\eta, V_{r_{ref}})} - \frac{1}{D(f_{\eta_{ref}}, V_{r_{ref}})} \right] R_{ref} f_t \right\} \\ & \times \exp\left\{ j \frac{4\pi K_m}{c^2} \left[1 - \frac{D(f_\eta, V_{r_{ref}})}{D(f_{\eta_{ref}}, V_{r_{ref}})} \right] \left[\frac{R_0}{D(f_\eta, V_r)} - \frac{R_{ref}}{D(f_\eta, V_r)} \right]^2 \right\}, \end{aligned} \tag{2.18}$$

where $W_r(f_t)$ is the range spectrum envelope or FFT of $w_r(t)$ in (2.13). The second phase multiplication in the CSA is the range matched filter, which is a 2-D filter with dependencies on both azimuth and range and is applied to all range-frequencies with a

dependence on f_η. The matched filter applies the bulk RCMC and SRC by removing the second and fourth exponential terms of (2.18) resulting in $S_3(f_t, f_\eta)$.

$$\begin{aligned} S_3(f_t, f_\eta) &= A_1 W_r(f_t) W_a(f_\eta - f_{\eta_c}) \\ &\times \exp\left\{-j\frac{4\pi R_0 f_0 D(f_\eta, V_r)}{c}\right\} \exp\left\{-j\frac{4\pi R_0}{cD(f_{\eta_{ref}}, V_{r_{ref}})} f_t\right\} \\ &\times \exp\left\{j\frac{4\pi K_m}{c^2}\left[1 - \frac{D(f_\eta, V_{r_{ref}})}{D(f_{\eta_{ref}}, V_{r_{ref}})}\right]\left[\frac{R_0}{D(f_\eta, V_r)} - \frac{R_{ref}}{D(f_\eta, V_r)}\right]^2\right\} \end{aligned} \tag{2.19}$$

The last step in range compression is to compute the 1-D inverse FT of $S_3(f_t, f_\eta)$ from f_t to t, returning it to the range Doppler domain

$$\begin{aligned} S_4(t, f_\eta) &= A_2 \rho_r\left(t - \frac{2R_0}{cD(f_{\eta_{ref}}, V_{r_{ref}}}\right) W_a(f_\eta - f_{\eta_c}) \exp\left\{-j\frac{4\pi R_0 f_0 D(f_\eta, V_r)}{c}\right\} \\ &\times \exp\left\{j\frac{4\pi K_m}{c^2}\left[1 - \frac{D(f_\eta, V_{r_{ref}})}{D(f_{\eta_{ref}}, V_{r_{ref}})}\right]\left[\frac{R_0}{D(f_\eta, V_r)} - \frac{R_{ref}}{D(f_\eta, V_r)}\right]^2\right\} \end{aligned} \tag{2.20}$$

where the range envelope $\rho_r(t)$ is the IFFT of $W_r(f_t)$ in (2.19). The signal $S_4(t, f_\eta)$ is now compressed in range with the range curvature corrected for all targets in the scene. Figure 2.7 shows the range compressed data in the range Doppler domain. For this scene, the amount of RCM is small and would only be noticeable in the full resolution scene data.

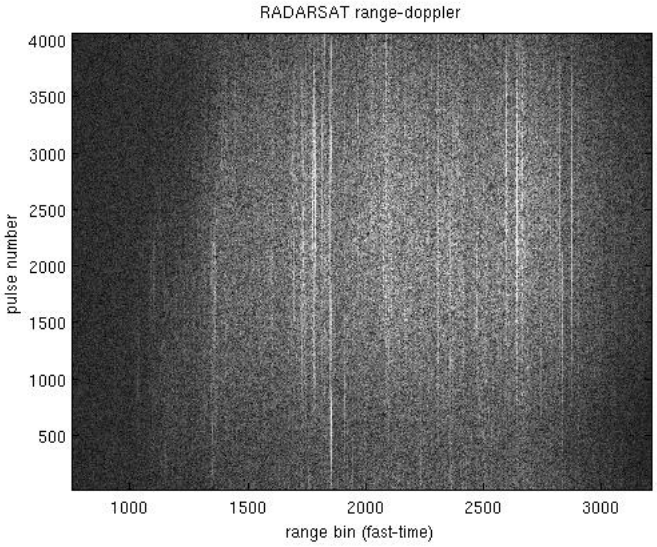

Figure 2.7: RADARSAT-1 range Doppler (Vancouver Airport BC).

Figure 2.8 plots the range cell migration throughout the processed aperture at the range reference location R_{ref}. As the plot indicates, the total RCM is 137 m and if we use $\rho_r = c/(2\text{BW})$ with the bandwidth $\text{BW} = 30.11$ MHz, then the range resolution is $\rho_r = 4.97$ m indicating the total RCM is ≈ 27 range-bins or pixels, which means the complete RCM of 27 pixels is spread across the 4096 samples of the azimuth array. This is a plot of the fourth exponential term in (2.18), thus it is the bulk RCMC.

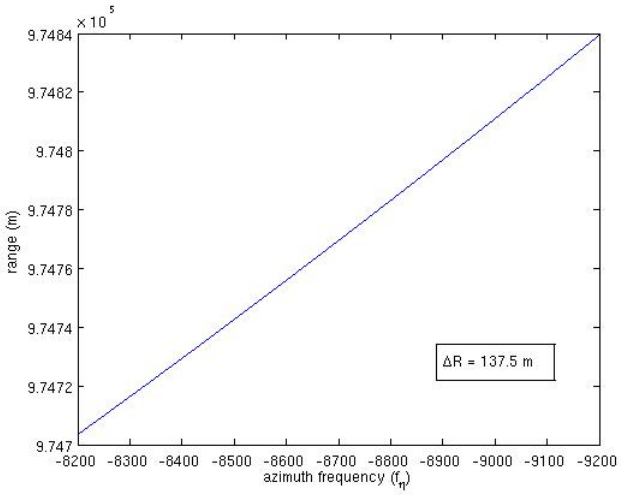

Figure 2.8: Range cell migration (Vancouver Airport BC).

2.5 Azimuth Compression

The third phase multiplication is the azimuth matched filter which is the conjugate of the first and fifth exponential terms of (2.18). The first term is the azimuth modulation and the fifth term the residual phase that is created in the first phase multiply (scaling function). After applying the range dependent azimuth matched filter, azimuth compression is completed with a 1-D inverse FT. As a result, the scene data is now compressed in both range and azimuth, providing a single look complex (SLC) image

$$S_5(t,\eta) = A_4 \rho_r \left(t - \frac{2R_0}{cD(f_{\eta_{ref}}, V_{r_{ref}})} \right) \rho_a(\eta - \eta_c) \exp\{j\theta(t,\eta)\} \tag{2.21}$$

where $\rho_a(\eta)$ is the IFFT of $W_a(f_\eta)$ in (2.20). There are different signal processing enhancements that are traditionally used in SAR processing but since we will be comparing performance with the FRFT, these enhancements will not be implemented but discussed in the conclusions.

2.6 Range Variant Scaling

The pervious section made an assumption that the transmitted pulse is an LFM chirp and both V_r and K_m are range invariant. In general, this is not the case in that V_r and K_m will vary in range providing higher order terms in the scaling function $s_{sc}(t, f_\eta)$. To account for these higher order terms, which are normally very small, we need a more general expression for the scaling function,

$$s_{sc}(t, f_\eta) = \exp\left\{ j2\pi \int_0^t K_m q_t(u, f_\eta) du \right\} \tag{2.22}$$

where

$$q_t(u, f_\eta) = \left[\frac{D(f_{\eta_{ref}}, V_r)}{D(f_\eta, V_r)} - 1 \right] t + \frac{2R_{ref}}{c} \left[\frac{D(f_{\eta_{ref}}, V_r)}{D(f_{\eta_{ref}}, V_{r_{ref}}) D(f_\eta, V_r)} - \frac{1}{D(f_\eta, V_r)} \right]. \tag{2.23}$$

To evaluate (2.22), the terms $K_m q_t(u, f_\eta)$ can be expanded as a power series around t. By assuming the frequency of the scaling function is locally linear, the function can be approximated as,

$$s_{sc}(t, f_\eta) = \exp\left\{ j \left[g_0 t + g_1 t^2 \right] \right\} \tag{2.24}$$

where the coefficients g_0 and g_1 vary with t and f_η. With this approximation, the residual phase (last term in (2.18)) is,

$$\phi_{res}(t, f_\eta) = \frac{4}{c^2} \frac{\pi K_m g_1}{\pi K_m + g_1} \left[\frac{R_0}{D(f_\eta, V_r)} - \frac{R_{ref}}{D(f_\eta, V_{r_{ref}})} + \frac{c g_0}{4 g_1} \right]^2 - \frac{g_0^2}{4 g_1}. \tag{2.25}$$

CHAPTER 3

Fractional Fourier Transform

3.1 Definition and Properties of the Fractional Fourier Transform

The fractional Fourier transform (FRFT) of order κ, $-2 \leq \kappa \leq 2$, is a generalization of the classical Fourier transform (FT), and it can be interpreted as a rotation by an angle $\alpha = \kappa\pi/2$ in the time-frequency (TF) plane. It can also be considered as a decomposition of the signal in terms of linear frequency-modulated (LFM) chirps [13, 22]. As a one-parameter subclass of the class of linear canonical transforms, most of the properties of the FRFT are special cases of the general properties of linear canonical transforms [23].

In Figures 3.1 and 3.2, we compare the FT and FRFT of an LFM chirp in the time-frequency (TF) plane. We see that the bandwidth of the LFM chirp signal in the FT domain is spread along the frequency axis as shown in Figure 3.1. If the TF plane is rotated using the FRFT with angle α, the energy distribution of the chirp is concentrated in the rotated domain, as shown in Figure 3.2 [18]. This rotation of the TF plane makes the FRFT an attractive transform to the signal processing community, especially for SAR signal processing and LFM detection. Specifically, the (t, f) coordinate system is rotated over an angle $\alpha = \kappa\pi/2$ counter clockwise, and the rotated variables are given by (u_α, v_α) in the TF plane in Figure 3.2. The variables can be obtained using the following rotation matrix or by applying the rotation operator $\mathscr{R}_\alpha$:

$$\begin{aligned} \begin{bmatrix} u_\alpha \\ v_\alpha \end{bmatrix} &= \begin{bmatrix} \cos\alpha & \sin\alpha \\ -\sin\alpha & \cos\alpha \end{bmatrix} \begin{bmatrix} t \\ f \end{bmatrix} \\ &= \mathscr{R}_\alpha(t, f) \end{aligned} \tag{3.1}$$

The rotated axes are obtained as

$$u_\alpha = t\cos\alpha + f\sin\alpha \tag{3.2}$$

$$v_\alpha = -t\sin\alpha + f\cos\alpha \tag{3.3}$$

and are more clearly demonstrated in Figure 3.3.

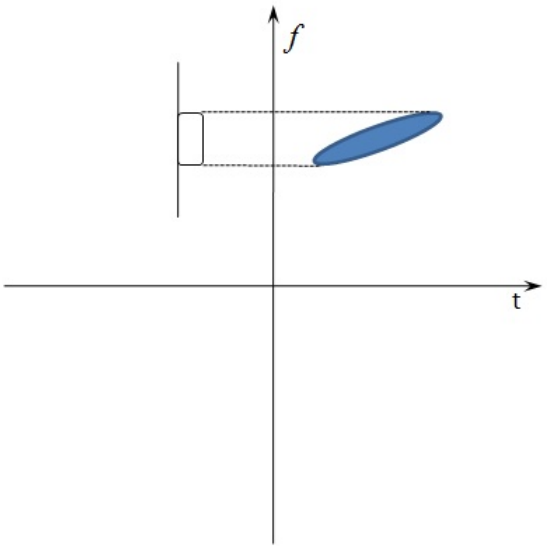

Figure 3.1: LFM projection in the TF plane.

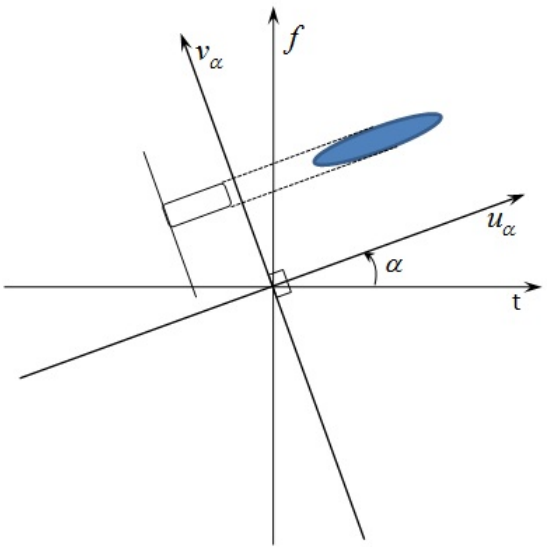

Figure 3.2: LFM projection in the rotated TF plane using the FRFT.

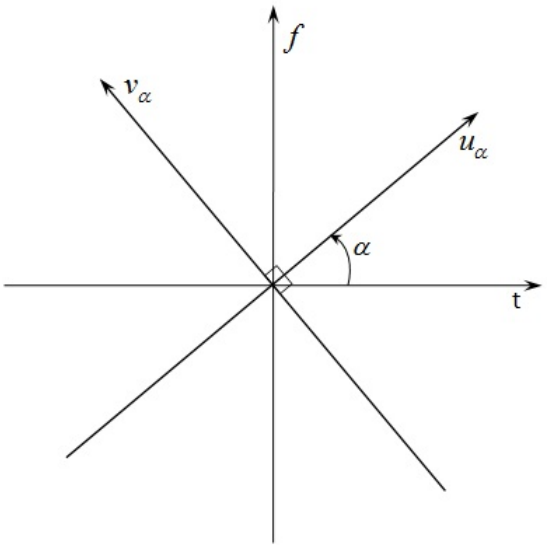

Figure 3.3: Fractional TF plane.

The continuous one-dimensional (1-D) FRFT is defined by means of the transformation kernel [12],

$$K(t,u_\alpha) = \begin{cases} \sqrt{1-j\cot\alpha}\, e^{j2\pi \frac{t^2+u_\alpha^2}{2}\cot\alpha - j2\pi u_\alpha t \csc\alpha}, & \text{if } \alpha \neq n\pi, n\in\mathbb{N} \\ \delta(t-u_\alpha), & \text{if } \alpha = 2\pi n, n\in\mathbb{N} \\ \delta(t+u_\alpha), & \text{if } \alpha = 2\pi n+\pi, n\in\mathbb{N} \\ e^{-j2\pi t u_\alpha}, & \text{if } \alpha = (\pi/2)n, n\in\mathbb{N} \end{cases} \tag{3.4}$$

For a continuous-time signal $x(t)$, the FRFT is thus defined as

$$X(u_\alpha) = (F^\alpha x)(u_\alpha) = \int_{-\infty}^{\infty} x(t)K(t,u_\alpha)dt \tag{3.5}$$

$$= \begin{cases} \sqrt{1-j\cot\alpha}\, e^{j2\pi \frac{u_\alpha^2}{2}\cot\alpha} \int_{-\infty}^{\infty} x(t) e^{j2\pi \frac{t^2}{2}\cot\alpha}\, e^{-j2\pi u_\alpha t\csc\alpha} dt, & \text{if } \alpha \neq n\pi, n\in\mathbb{N} \\ X(u_\alpha) = x(t), & \text{if } \alpha = 2\pi n, n\in\mathbb{N} \\ X(-u_\alpha) = x(-t), & \text{if } \alpha = 2\pi n+\pi, n\in\mathbb{N} \\ \int_{\infty}^{\infty} x(t)e^{-j2\pi t u_\alpha}dt = X(u_\alpha) = X(f), & \text{if } \alpha = (\pi/2)n, n\in\mathbb{N} \end{cases}$$

Given that F is the FT operator such that $(Fx)(f) = \int_{\infty}^{\infty} x(t)e^{-j2\pi tf}dt$ and F^{α} is the FRFT operator in Equation (3.5), then the FRFT possesses the following properties;

1. Zero rotation: $F^0 = I$ where $(Ix)(t) = x(t)$ is the identity operator
2. Consistency with the Fourier transform: $F^{\pi/2} = F$
3. Additivity of rotations: $F^{\beta}F^{\alpha} = F^{\alpha+\beta}$
4. 2π rotation: $F^{2\pi} = I$
5. Inverse FRFT: $(F_r^{\alpha})^{-1} = F^{(-\alpha)}$

where $(F^{\alpha})^{-1}F^{\alpha} = I$.

In addition, the FRFT kernel satisfies the following useful properties:

1. $K(t,u_{\alpha}) = K(u_{\alpha},t)$
2. $K(t,u_{-\alpha}) = K^*(t,u_{\alpha})$, where * indicates complex conjugation.
3. $K(-t,u_{\alpha}) = K(t,-u_{\alpha})$
4. $\int_{-\infty}^{\infty} K(t,u_{\alpha})K^*(t,\tilde{u}_{\alpha})dt = \delta(u_{\alpha}-\tilde{u}_{\alpha})$, where $\delta(u_{\alpha})$ is the Dirac delta function
5. $\int_{-\infty}^{\infty} K(t,u_{\alpha})K(u_{\alpha},z_{\beta})du_{\alpha} = K(t,z_{\alpha+\beta})$

Additional FRFT properties can be found in [12] and [23].

3.2 Relation of FRFT with Other Transforms

Consider a signal $x(t)$ and its FRFT $(F^{\alpha}x)(u_{\alpha})$. The Wigner distribution (WD) $W_x(t,f)$ of a signal $x(t)$ was defined in Equation (2.12) in Chapter 2 as

$$W_x(t,f) = \int_{-\infty}^{\infty} x\left(t+\frac{\tau}{2}\right)x^*\left(t-\frac{\tau}{2}\right)\exp(-j2\pi tf)d\tau.$$

The following relationship can be shown between the WD of the α FRFT of a signal and the rotated, over an angle $-\alpha$, of the WD of the same signal [23, 24]. Specifically,

$W_{x_\alpha}(t,f) = \mathscr{R}_{-\alpha} W_x(t,f) = W_x(t\cos\alpha - 2\pi f \sin\alpha, t\sin\alpha + 2\pi f\cos\alpha)$, where the rotation operator $\mathscr{R}_\alpha$ is defined in Equation (3.1).

Since several Cohen's class of time-frequency distributions are obtained by convolving a kernel characterizing the distribution with the Wigner distribution, an important relationship exists between the FRFT and those TFRs [24].

3.3 The Discrete FRFT

There are several challenges to the calculation of the FRFT; to date, there is no fast method similar to that of the FFT, however approximations have been proposed for both the discrete FRFT and continuous time transforms [12, 23, 24, 25, 26].

We need to introduce a new fractional operator F_r^κ that emphasizes the order κ of the FRFT rather than the angle α. It is thus related to the previous definition with $\alpha = \kappa\pi/2$ or

$$F_r^{\kappa\pi/2} = F^\alpha \text{ or } F_r^1 = F^{\pi/2} = F. \tag{3.6}$$

The new operator F_r^κ has the same properties as F^α and will be used as the operator for the discrete approximation to the FRFT.

Figure 3.4 provides two different views of an FRFT of a rectangular signal with $N = 64$ samples, which sweeps the FRFT order $0 \leq \kappa \leq 1$. As mentioned in Section 3.1, the FRFT is periodic in 2π, and it is also symmetric about $\pi/2$ with strong oscillations as α approaches 0 or π. In Figure 3.4 we notice strong oscillations for $\kappa < 0.5$ and the expected sinc pattern for $\kappa = 1$, which is in agreement with the FT property $F_r^1 = F$.

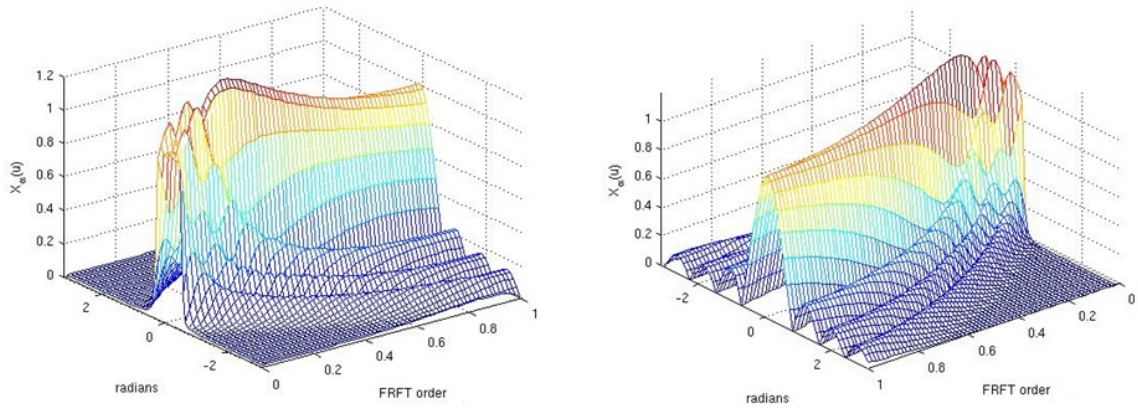

Figure 3.4: Two different views of the FRFT of a rectangular signal.

A definition of the discrete FRFT (DFRFT) is provided in [27] which generalizes the definition of the discrete FT (DFT) in the same manner as the continuous fractional FRFT generalizes the continuous FT. This definition of the DFRFT is based on a set of eigenvectors of the DFT matrix, which consist of the discrete counterparts from the set of Hermite-Gaussian functions. It satisfies the following desirable properties: (a) the DFRFT is a unitary transform; (b) it preserves the additivity property $F^b F^a = F^{a+b}$; (c) it reduces to the DFT when the order is unity; and (d) it approximates to the continuous FRFT.

A fast $O(N \log_2 N)$ approximation for computing the continuous FRFT is provided in [25] which maps the N samples of the original signal to N samples of the FRFT. The FRFT of an arbitrary signal $x(t)$, with angle α, is defined in Equation (3.5). In particular, for angles that are not multiples of π, the computation of the FRFT corresponds to the following steps: (a) the signal is first multiplied by an LFM chirp; (b) the FT of the signal product is computed; (c) perform some scaling; (d) multiply by an LFM chirp.

Two methods for computing the approximation are provided in [25]. One method

which does not include the use of Fresnel integrals is,

$$(F_r^{\kappa}x)\left(\frac{m_{\kappa}}{2\Delta x}\right) = \frac{A_{\alpha}}{2\Delta x}e^{i2\pi(\rho-\beta)(m/2\Delta x)^2}\sum_{n=-N}^{N}e^{i2\pi\beta((m-n)/2\Delta x)^2} \times e^{i2\pi(\rho-\beta)(n/2\Delta x)^2}x\left(\frac{n}{2\Delta x}\right) \tag{3.7}$$

where $\alpha = \kappa\pi/2$, $\rho = \cot\alpha$, $\beta = \csc\alpha$ and

$$A_{\alpha} = \frac{\exp(-j\pi\mathrm{sgn}(\sin\alpha)/4 + j\alpha/2)}{|\sin\alpha|^{1/2}}$$

Since the summation in (3.7) is recognized as a convolution, the algorithm can be computed with an FFT providing the FRFT with complexity $O(N\log_2 N)$.

The result of the first chirp multiplication with x will cause a shearing in the TF plane, making the bandwidth or time-bandwidth product twice as large. Since this is twice the original support, x will need to be interpolated or up-sampled containing at least $2N$ samples [26]. It will be assumed that this interpolation was done before x is used in (3.7). For more detailed discussions of shearing in the TF plane see Appendix A of [25] with an additional derivation in [23]. Also, the convolution of x with a chirp will cause a similar shearing; see [20] for an additional discussion on the effect of time-frequency distributions.

As noted and displayed in Figure 3.4, the FRFT exhibits strong oscillations as κ approaches 0 or 2. To adequately sample the FRFT in these regions would drive complexity, so (3.7) is restricted to $0.5 \leq |\kappa| \leq 1.5$. There are different routines using the fractional additivity property to work around this constraint of limiting $\kappa \in [0.5, 1.5]$. For $\kappa \in [0,2]$, the method provided in [25] is,

1. If $0.5 \leq \kappa \leq 1.5$ or $2.5 \leq \kappa \leq 3.5$, evaluate the integral directly

2. If $-0.5 \leq \kappa \leq 0.5$ or $1.5 \leq \kappa \leq 2.5$ then $F^{\kappa} = FF^{\kappa-1}$

3.3.1 *FRFT Implementation in* MATLAB

There are two MATLAB programs available for computing (3.7), which are freely available on the web. The first is *fracF* and can be obtained at the website for the book [23]. The second is *fracft* and is distributed as a routine within the MATLAB time-frequency toolbox *DiscreteTFDs*, developed by J. O'Neill. A complete analysis of the two routines is provided in [26] and will not be covered here, however the difference in their implementations will drive a decision to use *fracF* for the implementation in Chapter 6.

The main difference is that *fracF* operates on an even number of samples and uses FFTs for upsampling in (3.7). The *fracft* routine operates on an odd number of samples and uses sinc interpolator for upsampling. The sinc interpolator is defined as $x(t) = \sum_{n=-\infty}^{\infty} x_n \text{sinc}\left(\frac{\pi}{T}(t-nT)\right)$ where T is the sampling period and $\text{sinc}(x) = \sin(x)/x$, for $x \neq 0$ and $\text{sinc}(0) = 1$ [28]. It is noted in [26] that *fracft* provides slightly improved results due to the symmetric kernel, however the odd number of samples will be problematic for optimized FFT sizes needed in implementation.

CHAPTER 4

Linear Frequency-Modulated Chirp Detection

4.1 Fractional Autocorrelation Function

As the fractional Fourier transform (FRFT) is a linear canonical transformation [15], it can be associated with a fractional autocorrelation function (FrACF). That is an important function, for example, in estimating the rate of linear frequency-modulated (LFM) chirps using one-dimensional (1-D) searches, especially at low signal-to-noise ratios (SNRs) [15, 16, 17]. Using a fast discrete FRFT approximation, the 1-D searches can replace the more computationally intensive 2-D ambiguity function (AF) searches since the FrACF at an arbitrary angle corresponds to a radial slice of the AF passing through its origin at the same arbitrary angle [15].

Consider a continuous-time signal $s(t)$ and the unitary and Hermitian fractional operation $(R_\rho^\alpha s)(t)$ presented in [15] as

$$(R_\rho^\alpha s)(t) = s(t-\rho\cos\alpha)e^{-j2\pi t\rho\sin\alpha}e^{j\pi\rho^2\cos\alpha\sin\alpha}.$$

Using the fractional operation, the FrACF, $\mathrm{FA}^\alpha(\rho)$, of $s(t)$ is simply the correlation between the signal $s(t)$ and its fractionally operated signal in the time domain. Specifically, the FrACF is given by[2],

$$\mathrm{FA}^\alpha(\rho) = \langle s, (R_\rho^\alpha s)\rangle = e^{j\pi\rho^2\cos\alpha\sin\alpha}\int s(t)s^*(t-\rho\cos\alpha)e^{-j2\pi t\rho\sin\alpha}dt. \tag{4.1}$$

Two special cases of the FrACF are obtained for $\alpha = 0$ and $\alpha = \pi/2$, and are given by

$$\mathrm{FA}^0(\rho) = \int s(t)s^*(t-\rho)dt \tag{4.2}$$

$$\mathrm{FA}^{\pi/2}(\rho) = \int |s(t)|^2 e^{-j2\pi t\rho}dt = \int S(f)S^*(f-\rho)df \tag{4.3}$$

where $S(f)$ is the conventional Fourier transform (FT) of $s(t)$. The FrACF can also be expressed in terms of the AF, $\mathrm{AF}_s(t,\nu)$, of the signal $s(t)$ or its FRFT, $(F_r^\alpha s)(t) = S(u_\alpha)$

[2]Unless otherwise indicated, all integration limits are from -infinity to infinity.

in Equation (3.5). These two relationships are given as [16],

$$\mathrm{FA}^{\alpha}(\rho) = \mathrm{AF}_s(\rho\cos\alpha, \rho\sin\alpha) \tag{4.4}$$

$$= \int S(u_\alpha) S^*(u_\alpha - \rho) du_\alpha \tag{4.5}$$

where the AF of $s(t)$ is defined as

$$\mathrm{AF}_s(\tau, \upsilon) = \int s\left(t + \frac{\tau}{2}\right) s^*\left(t - \frac{\tau}{2}\right) e^{-j2\pi\upsilon t} dt. \tag{4.6}$$

The relationship between the FrACF and the AF in Equation (4.4) shows that the FrACF at angle α is equivalent to radial (of value ρ) slices of the AF, evaluated along the orientation α. This relationship is similar to the one that the time-correlation in (4.2) shares with $\mathrm{AF}_s(t,0)$, which is a slice of the AF, evaluated along the horizontal axis. Equation (4.4) will be exploited in the next section, for detecting LFM chirps.

Assuming a signal duration of N samples, an efficient method for calculating the FrACF is given in [16], using a fast $O(N\log_2 N)$ approximation of the FRFT [25]. The method makes use of another approach to compute the FrACF by taking the inverse FT of the squared magnitude of the FRFT of the signal $s(t)$ with the orthogonal angle parameter $\theta_\alpha = \alpha + \pi/2$. Specifically, we can re-write (4.1) as

$$\mathrm{FA}^{\alpha}(\rho) = \int |S(u_{\theta_\alpha})|^2 e^{j2\pi\rho\theta_\alpha} d\theta_\alpha. \tag{4.7}$$

The efficient FrACF implementation follows from the discrete-time approximation of Equation (4.7) [15]. Specifically, with M different angles α_m, $m = 1,\ldots,M$, the FrACF can be effectively implemented by first uniformly sampling the signal $s(t)$ using the sampling period T_s to obtain the samples $s[n] = s(nT_s)$, $n = 1,\ldots,N$; then the FRFT can be calculated at orthogonal angles $\alpha_m + \pi/2$ for the sampled signal using the discrete FRFT in [25]; the squared-magnitude $s[n]$ of the FRFT is computed, and then its inverse FT is obtained to yield the FrACF of the signal.

4.2 LFM Detection Accuracy

A motivation for LFM estimation in SAR signal processing is to reduce the frequency-modulation (FM) mismatch between the expected and received waveforms due to non-linear motion between the radar and target [8, 18, 29]. In doing so, the fractional optimization operators are used to tune the FRFT to produce an optimal response in pulse compression, providing an increased SNR and improved peak sidelobe ratio (PSLR) performance. To characterize the FM estimation accuracy, the Cramér-Rao lower bound (CRLB) is used as the threshold for estimation performance [30].

Consider a received signal of the form,

$$s(t) = A\exp[j\pi(Kt^2 + f_0 t)] + w(t), \qquad -T_d/2 < t < T_d/2 \tag{4.8}$$

where T_d is the signal duration, A is the amplitude, K is the FM rate, f_0 is the initial frequency and $w(t)$ is zero mean complex additive white Gaussian noise (AWGN). The mean squared error (MSE) of the FM rate estimation is given by [17],

$$\text{MSE} = \frac{1}{B}\sum_{l=b}^{B}(K_b - K)^2 \tag{4.9}$$

where B is the number of Monte Carlo simulation trials, K_b is the estimated FM rate at the bth simulation and K is the true FM rate. The CRLB for an unbiased FM rate MSE estimator is given by [17],

$$\sigma_K^2 = \frac{90 f_s^4}{2\pi^2 N(N^2-1)(N^2-4)\text{SNR}} \tag{4.10}$$

where f_s is the sampling frequency, N is the number of samples and the SNR is A^2/σ^2, where σ^2 is the variance of the real and imaginary parts of the complex noise (note, the real and imaginary parts have equal variances). As indicated in [17], the matched filter (MF) detector and generalized likelihood ratio test (GLRT) detector provide better estimation performance, especially in low SNR environments. For our simulations, we

compare the FrACF based detector with the GLRT detector [31].

4.2.1 GLRT Detector

The GLRT statistic for the received signal in Equation (4.8) first computes the maximum likelihood estimate (MLE) of the unknown FM rate K. As the MLE cannot be computed in closed form [31], it is given by

$$K_{\mathrm{MF}} = \arg\max_{K} C \int |S(f) \int e^{-j\pi(Kt^2+f_0t)} e^{-j2\pi tf} dt| e^{j2\pi tf} df. \tag{4.11}$$

The typical definition of a matched filter is a correlator that will maximize the correlation SNR. For the statistic provided in (4.11), instead of maximizing the correlation SNR, we will maximize the correlation contrast, where contrast is defined as the ratio of the standard deviation over the mean of the pixel magnitudes [9]. For SAR processing, contrast is a common image quality metric normally calculated over a spatial region in an image with pixels contained in a 2-D array encompassing the spatial region. For the test statistic provided in (4.11), contrast will be calculated using the 1-D signal S(f).

$$C = \frac{E(|I|^2)}{[E(|I|)]^2} \tag{4.12}$$

where I is the pixel magnitude and $E(\cdot)$ is statistical expectation.

For the maximization procedure in (4.11) to estimate the FM rate, we will use the golden search algorithm to reduce the computational burden of sweeping from the lower to upper bounds [32]. The golden search algorithm will always find a minimum or maximum value, however it can converge at local extrema. To help reduce the number of iterations and avoid converging on local extrema, it helps to constrain bounds of the search parameters to known limits. This can be done by first using a course resolution search, choosing its maximum value, and then using it as input to the golden search. Note that we also use the same search algorithm for the FrACF optimization.

4.2.2 *Fractional Autocorrelation Function Detector*

For the LFM signal in (4.8), if both the FM rate K and the initial frequency f_0 are unknown, then the optimal GLRT detector can be obtained by integrating all possible lines in the Wigner distribution time-frequency plane [33]. If f_0 is not a parameter of interest or is known, then a different detector was proposed in [16], that is based on the AF of the received signal. Specifically, the detector uses the fact that all LFM chirp signals have a linear support region that crosses the origin of the AF, thus minimizing the region of search for the estimated FM rate. The detector then becomes the integration of the magnitude of the AF along lines that only go through the origin in the AF plane. Specifically, the estimated FM rate is,

$$K_{\text{AF}} = \arg\max_{K} \int |\text{AF}_s(t, Kt)| dt \tag{4.13}$$

which is the maximization of all line integrals of the AF along lines whose slopes correspond to any possible values of the FM rate K.

In order to simplify the computation of the 2-D search in the AF plane in (4.13), the relation between the AF and FrACF in Equation (4.1) is used. Specifically, from (4.13), the line in the AF plane is given by $\nu = Kt$ and has slope K. If we assume that this radial line makes an angle α going through the origin, then a different equation can be written for the integral of the AF in (4.13), that makes this angle $\alpha = \tan^{-1}(K)$. This integral is given by,

$$\int \int |\text{AF}_s(t, \nu)| \delta(\nu \cos\alpha - t \sin\alpha) dt \, d\nu \tag{4.14}$$

and it can be further simplified to,

$$\int |\text{AF}_s(t\cos\alpha, t\sin\alpha)| dt. \tag{4.15}$$

Using (4.4), the integral can also be written in terms of the FrACF of the signal $s(t)$ as,

$$L(K) = \int |\mathrm{FA}^{\tan^{-1}(K)}(\rho)| d\rho. \tag{4.16}$$

As a result, the detector will maximize this FrACF equation, over all possible values of K,

$$K_{\mathrm{FrACF}} = \arg\max_K L(K) = \arg\max_K \int |\mathrm{FA}^{\tan^{-1}(K)}(\rho)| d\rho. \tag{4.17}$$

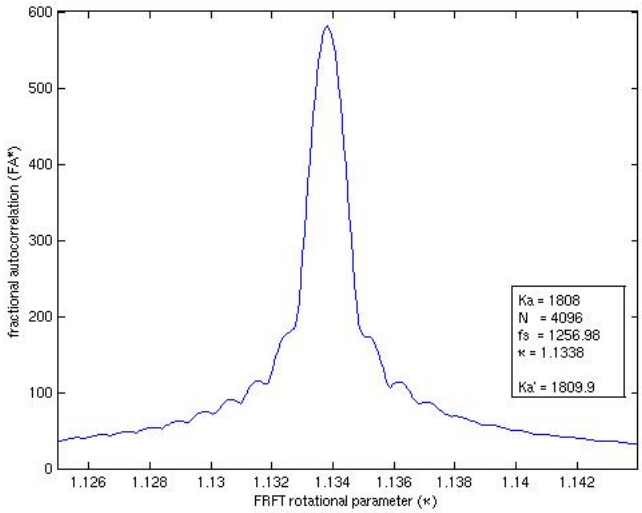

Figure 4.1: Plot of FrACF detector statistic $L(K)$ in (4.17) for different $\alpha = \tan^{-1}(K)$, where $\alpha = \kappa\pi/2$. The true LFM rate is $K_a = 1808$ and the estimated one is $K_a' = 1807.9$.

Figure 4.1 is a plot of the FrACF estimate provided by (4.17) with the lower and upper FRFT order κ constrained between 1.125 and 1.143.

Since we are interested in FM rate estimation, we will be using (4.8) with $A = 1$ and $f_0 = 0$. The range matched filter parameters are provided in Table 4.1 and azimuth matched filter in Table 4.2.

Table 4.1: Range matched filter parameters

Parameter	Symbol	Value	Units
Sampling rate	f_s	32.317	MHz
Range FM rate	K_r	721.35	GHz/s
Pulse duration	T_r	41.74	μs
Number of range samples	$N_r = f_s T_r$	1349	samples

Table 4.2: Azimuth matched filter parameters

Parameter	Symbol	Value	Units
Approximate FM rate	K_a	1800	Hz/s
Pulse repetition frequency (PRF)	F_a	1256.98	Hz
Pulse duration	T_a	0.56	s
Number of range samples	$N_a = F_a T_a$	705	samples

The relationship between the FRFT rotational parameter α and the FM rate of a discretely sampled signal is given in [34]. For an LFM chirp $e^{j2\pi(zt^2+bt+c)}$, with instantaneous frequency $2zt+b$, the optimal FRFT order parameter is,

$$\kappa_{\text{opt}} = \frac{2}{\pi}\alpha_{\text{opt}} = -\frac{2}{\pi}\tan^{-1}\left(\frac{\delta f/\delta t}{2z}\right) \tag{4.18}$$

where (a) $\delta f = f_s/N$ is the frequency resolution; (b) δt is the time resolution; (c) f_s is the sampling frequency; and (d) N is the number of samples. Thus we can re-write (4.18) as

$$\kappa_{\text{opt}} = \frac{2}{\pi}\alpha_{\text{opt}} = -\frac{2}{\pi}\tan^{-1}\left(\frac{f_s^2/N}{2z}\right) \tag{4.19}$$

The FM rate statistic provided by (4.17) and the GLRT statistic provided by (4.11), were generated using 200 Monte-Carlo simulations. For the comparison results shown next, the FM rate estimation MSE is plotted in dB using $10\log_{10}\left(\frac{1}{\text{MSE}}\right)$ with signal SNR spanning -5 to 20 dB.

4.2.3 RADARSAT LFM detection accuracy

In this section, simulations are performed with RADARSAT-1 LFM parameters provided in tables 4.4 and 4.2 to characterize the FrACF detector performance in varying SNR. We use the results of this chapter to require a minimum SNR for LFM detection using real RADARSAT-1 data in Chapter 6. Figure 4.2 is a plot of the simulations and it indicates that for the RADARSAT-1 range parameters, the FrACF has good estimation performance for SNRs above approximately 7 dB. The performance of the GLRT is better for low SNR environments, as expected from [17]. To use the FRFT for autocorrelation or other applications requires the signal to be compact in the fractional domain, meaning all energy must be contained within a constant radius in the Wigner distribution [25]. To assure compactness, $s(t)$ is over-sampled, increasing the number of samples N, from 1349 to 4096, which corresponds to a good size for FFT. The CRLB is provided using the original number of samples which could explain the slightly improved MSE performance for the FrACF method. The standard deviation σ of the FM rate estimate is provided in Figure 4.3 and is in agreement with the MSE plot. This parameter is necessary for the expected FM rate mismatch when using the estimated rate in SAR focusing applications.

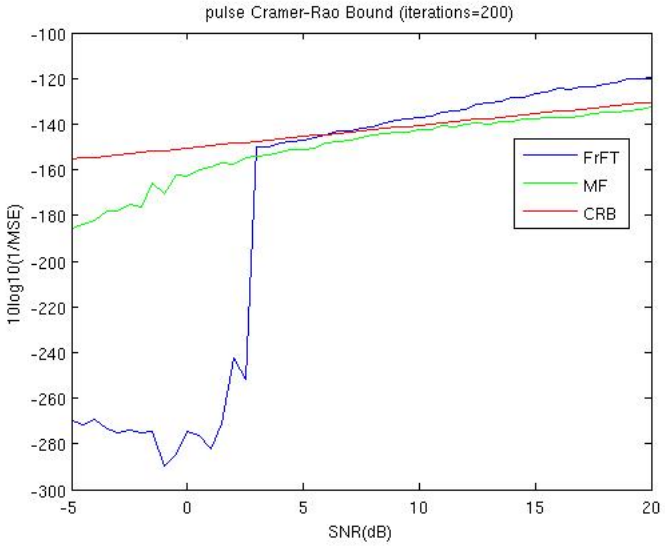

Figure 4.2: Range FM rate estimation ($N = 1349$, $K_r = 721.4$ GHz/s (see Table 4.1)).

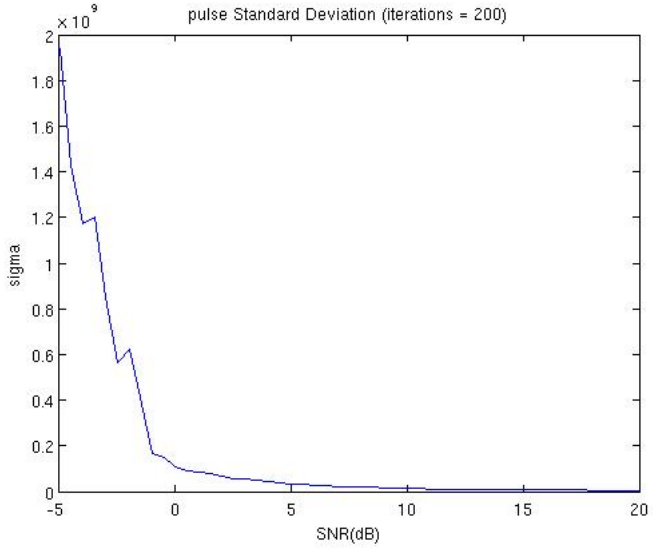

Figure 4.3: Range standard deviation FM rate estimation.

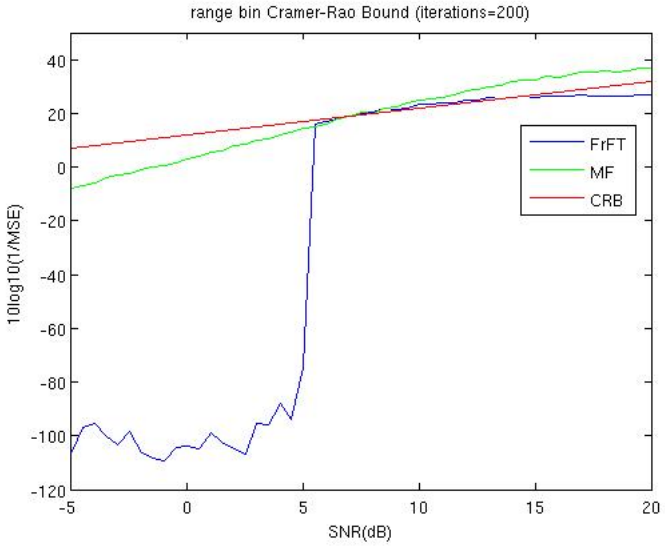

Figure 4.4: Range bin FM rate estimation ($N = 705$, $K_a = 1808$ Hz/s (see Table 4.2)).

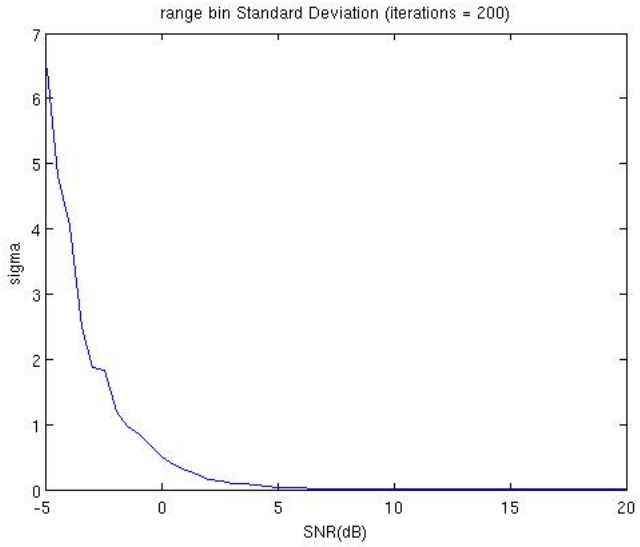

Figure 4.5: Azimuth standard deviation azimuth FM rate estimation.

Figure 4.4 indicates that the performance for the azimuth estimation is similar to that of the range: an abrupt change in estimation error for SNRs above 5 dB and, as expected, a better estimation of performance for the GLRT in low SNR environments.

Figure 4.6 is a plot of the receiver operating characteristics (ROC) for the azimuth FM rate or the rate of each range bin. The same detection statistic as provided in (4.17) was used, with the exception that the maximum value of the FrACF estimate was used instead of the sweep rate as depicted in Figure 4.1. To generate the ROC curves, 250 simulations were performed for different SNRs and the curves were produced using [31],

$$P_D = Q\left(Q^{-1}(P_{FA}) - \sqrt{NA^2/\sigma^2}\right) \tag{4.20}$$

where $A = 1, N = 256$ and σ^2 was estimated from the simulation runs for each SNR.

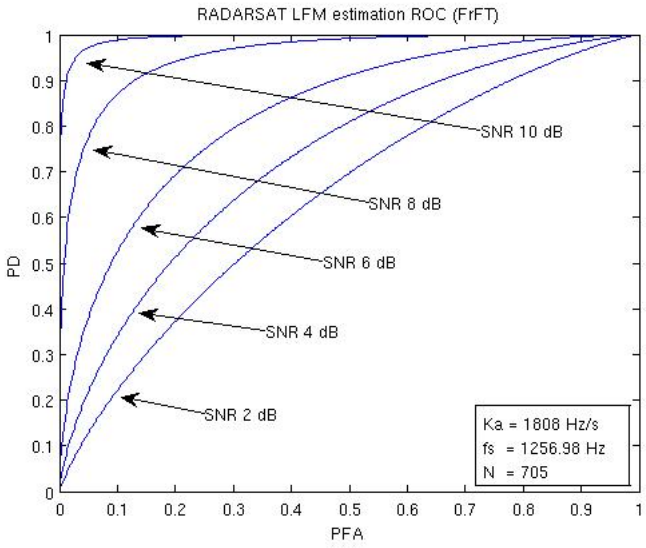

Figure 4.6: Azimuth FrACF ROC.

4.2.4 RADARSAT FRFT FM Rate Detection Resolution

For completeness, we wanted to include this section on the FM rate resolution capability of the FRFT, with resolution defined as the ability to distinguish between two equally strong LFM signals in a noise-free environment [33]. We will not be addressing multi-component LFM signals any further but wanted to include this because of its dependence on LFM accuracy and its use in SAR signal processing, specifically in the areas of moving target detection and inverse synthetic aperture radar (ISAR) [35, 36]. For

conventional SAR, the radar antenna moves in relation to the target, whereas for ISAR, the antenna is stationary and the target moves to form the synthetic aperture.

It is noted in [35] that the ability to separate two chirp signals with very small difference in chip rate has not been well defined, but simulations reveal that resolution is inversely proportional to the square of the signal length T_d. A recent work [37] provides an algorithm which we will use to estimate the minimum resolution but also cites the lack of any comparative studies.

For multi-component signals of the form [37],

$$s(t) = \sum_{m=1}^{M} A_m \cos(2\pi f_{0m} t + \pi K_{0m} t^2) + w(t), \qquad -T_d/2 \leq t \leq T_d/2 \tag{4.21}$$

where M is the number of LFM components, A_m is the amplitude of the mth LFM signal and $w(t)$ is zero-mean white Gaussian noise. The minimum resolution capability of the FRFT is provided by,

$$\Delta K_{\min} = \left| \frac{2\csc(\cot^{-1}(K_0 T_d / f_s))}{T_d^2} \right| \tag{4.22}$$

where $\Delta K_{\min}$ is the difference between the upper and lower lines of a parallelogram created in the normalized TF plane by two LFM signals with the same center frequency f_0. The axis normalization is achieved by first defining the scaling variable $s = \sqrt{\Delta t / \Delta f}$, then creating the normalized axis $x = \Delta t / s$ and $\nu = f_s s$. The length of both axes is now represented by the dimensionless value $\sqrt{\Delta t \Delta f}$ depicted as Δx in Figure 4.7. Additional details of TF axis normalization can be found in [23, 25].

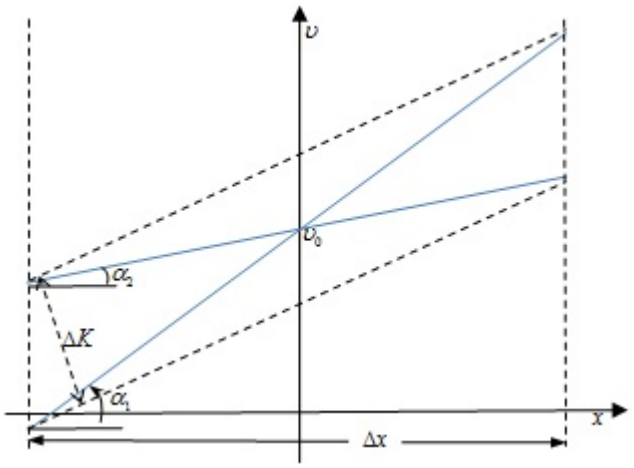

Figure 4.7: Multi-component TF plane (normalized axis).

Figure 4.8 plots $\Delta K_{\min}$ as provided by (4.22) for different up-sampling ratios.

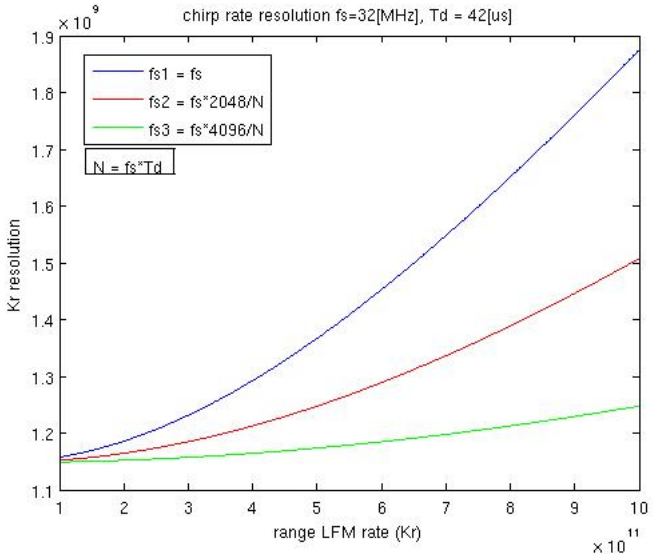

Figure 4.8: Minimum detectable range resolution.

Figure 4.9 is a MATLAB simulation using the same range LFM values as in the previous section to include the up-sampling of the signal to an FFT size of 4096. The multi-component signal was created using (4.21) with $M = 2,\ A_m = 1$ for all m, $f_{0m} = 0$, for all m and $w(t) = 0$ for all t, and for the FM rates, $K_{01} = K_r$ and $K_{02} = K_r + K_r'$.

The FrACF plot in Figure 4.9 (left) shows good FM rate separability for $\Delta K \geq 3.2$GHz/s and the FrACF plot Figure 4.9 (right) shows the inability to separate FM rates for $\Delta K \leq$ 3.0GHz/s.

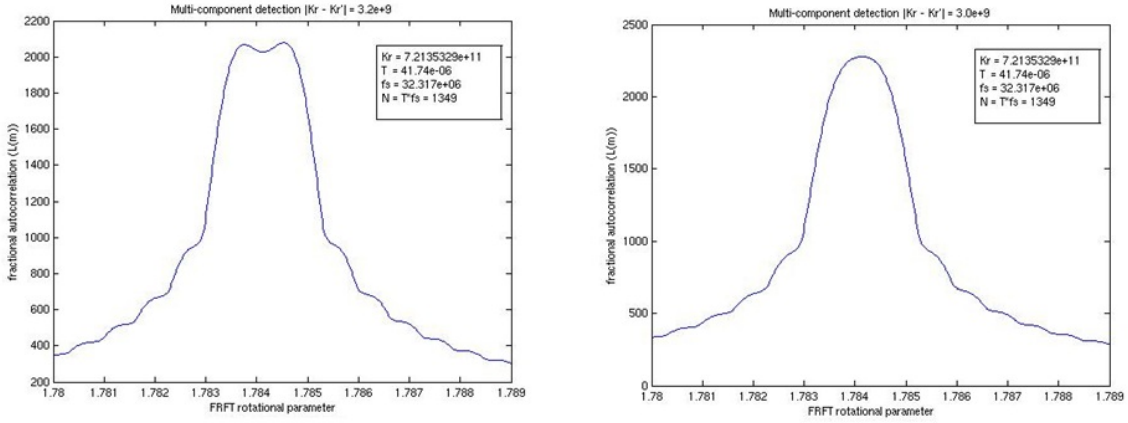

Figure 4.9: Multi-component detection, $N = 4096$.

CHAPTER 5

Fractional Focusing and the Chirp Scaling Algorithm

5.1 Fractional Chirp Scaling Algorithm (FrCSA)

The fractional Fourier transform (FRFT) has found widespread acceptance within the synthetic aperture radar (SAR) signal processing community, mainly in operations of linear frequency-modulated (LFM) chirp detection, high profile range imaging (inverse synthetic aperture radar (ISAR)) [8, 38] as well as single channel SAR images for the detection of moving targets [18]. A common thread to the mentioned algorithms is the detection of chirp type signals amongst random clutter. Most recently, fractional chirp scaling algorithm (FrCSA) approaches have been investigated [2, 39] with improved signal-to-noise ratio (SNR) and greater sidelobe reduction, when compared with previous implementations of the chirp scaling algorithm (CSA). Typical sidelobe mitigation strategies in SAR image processing make use of weighting functions, however this method causes an unwanted boarding of the impulse response width (IRW) and degradation of SNR. If the sidelobes can be reduced without the use of weighting functions, then the IRW and SNR degradations may be avoided, yielding improved performance for the FrCSA.

The new FRFT based CSA uses the FRFT to enhance the overall focusing capabilities of the CSA [2]. A flow diagram of the algorithm is provided in Figure 5.1. The algorithm makes use of a local optimization procedure (LOP) [2] that investigates all possible FRFT rotation angles α and selects the optimum value to be used throughout the algorithm.

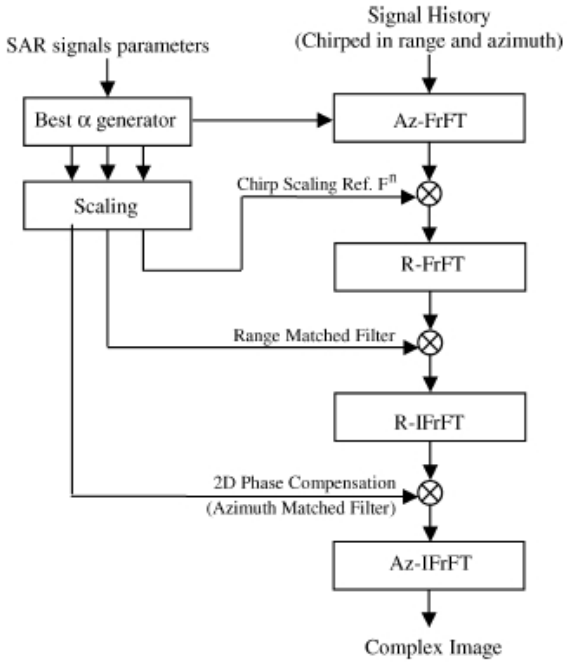

Figure 5.1: Block diagram of FrCSA algorithm. Here R denotes range, and Az denotes azimuth. Figure taken from [2].

The most important steps in the FrFT is in range transformation processing and the fractional correlator-based range match filter [40]. A module combining these two steps gives the FrCSA its unique strength relative to the Fourier transform (FT) based CSA in handling signals, particularly at the far end of the scene.

5.2 Fractional Focusing with Contrast Maximization

The intent of this research is to understand how the FRFT can be used in SAR signal processing, specifically as part of the CSA algorithm, to improve image formation. Using the relationship of the FRFT with time-frequency (TF) representations [12], we began by analyzing the Wigner distributions (WDs) of range-bin samples and the corresponding matched filter to understand how the rotational parameter of the FRFT could tune the transform to produce an optimal pulse compression response. Figure 5.2 shows plots of

the match filter (upper plot) and the range-bin signal (lower plot) for range-bin 969. As expected, the signals are conjugates of each other and matched filtering should concentrate the energy to discrete frequencies with narrow bandwidth. This method will only apply to stationary targets. Moving targets will not be localized in frequency but walk across frequencies [7], maintaining a slope or ramp, thereby maintaining bandwidth in the TF plane.

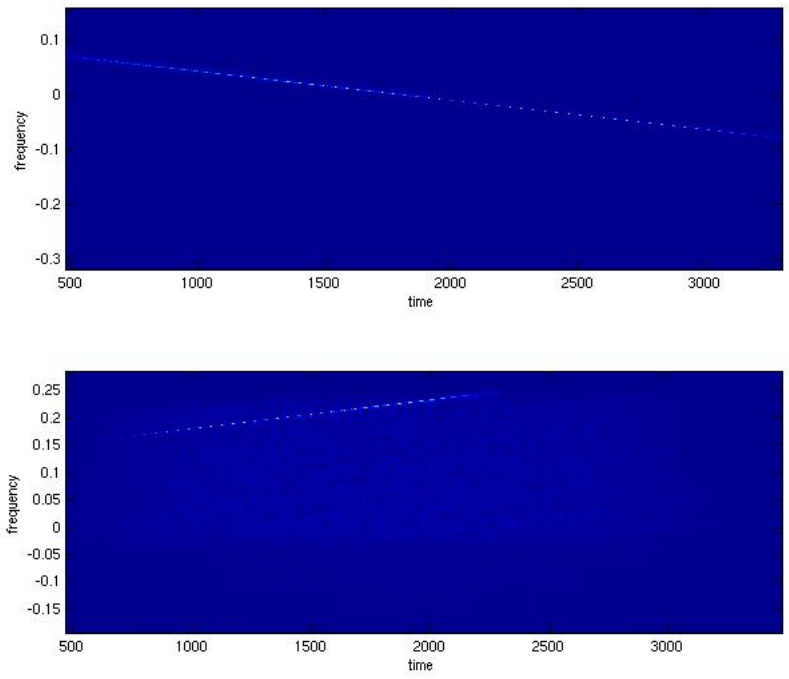

Figure 5.2: Wigner distribution representations of matched filter and range-bin signals.

The upper plot in Figure 5.2 is the WD of the pulse after matched filtering, using the classical FT, with the fractional order set to 1, $(F_r^1 x)(f)$, and the lower plot is the result of tuning the transform with $(F_r^\kappa x)(f_\kappa)$ where $\kappa = -0.001386$ and is related to the rotational parameter $\alpha = \kappa\pi/2$. We see that with optimal parameter selection, the energy or target after match filtering is concentrated in frequency with narrow bandwidth for the optimized center frequency. As the WD indicates, the resulting signal is a frequency domain signal

and an inverse FT will rotate it by $\pi/2$ concentrating the target in time.

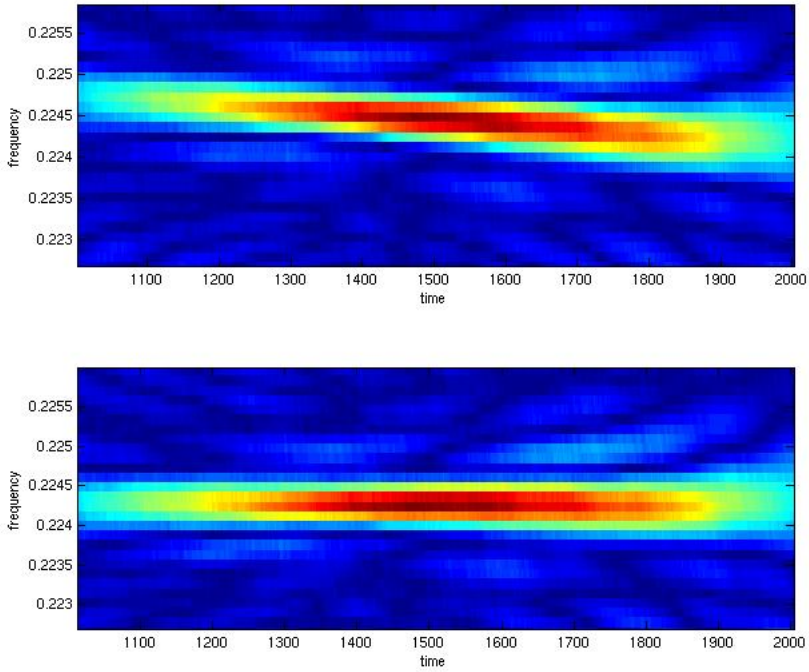

Figure 5.3: (WD) or pulse after matched filtering: using classical FT (upper plot) and optimized with FRFT optimization (lower plot).

Figure 5.4 is a comparison of the target response for range-bin 969, comparing the FT and FRFT methods. We see the FRFT response has an improved peak-to-sidelobe ratio (PSLR) with better concentration of the target energy. To obtain the optimized value $\kappa = -0.001386$, we computed the MLE in (4.11) with contrast maximization as the selection criteria.

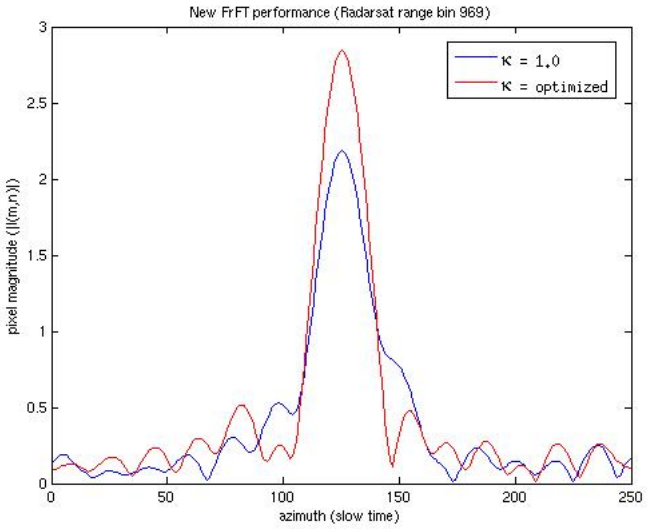

Figure 5.4: Comparison of target response for range-bin 969 using classical FT (F_r^1) (blue-line) and optimized FRFT (F_r^{κ}) (red-line).

Recent works have indicated that the FRFT can be used to correct mismatches between the expected and the received signal's FM rate [2, 8, 18]. This mismatch can be explained as a nonlinear motion between the platform and target. To understand the optimization capabilities of the FRFT with mismatches in the expected FM rate, we conducted a sweep of the azimuth FM rate K_a while maximizing the contrast using the FRFT. The same contrast maximization method was provided in (4.11), with the exception that the FRFT rotational parameter is also swept between κ_{min} and κ_{max} creating a 2-D search.

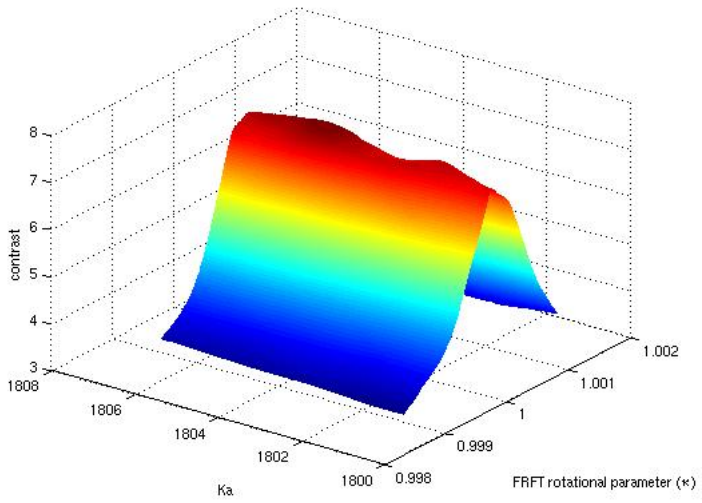

Figure 5.5: MATLAB mesh plot of 2-D contrast maximization search; sweeping K_a and κ.

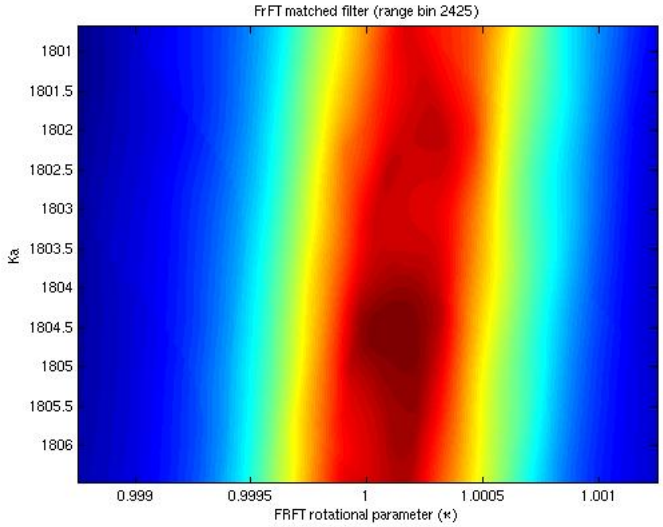

Figure 5.6: MATLAB scaled image of 2-D search, highlighting maximum contrast at: $Ka = 1804.5$ and $\kappa = 1.0002$.

Figures 5.5 and 5.6 indicate that the FRFT was able to maximize the contrast for each FM rate, however the absolute maximum occurs with a K_a mismatch that is less then 0.01

percent of the optimal FM rate. We also notice that the absolute maximum occurred for the rotational value $\kappa = 1.0002$ indicating that for this signal, the FRFT enhanced the PSLR beyond that of the MLE search methods.

5.3 Fractional Focusing and the CSA

To apply the fractional focusing method of the previous section, it is necessary to modify the CSA in Figure 2.2 so FRFT optimizations can be implemented. There are two common approaches for FRFT optimization [2, 34]. The first approach chooses a global FRFT order κ and uses it for all pulses or range-bins processed with the FRFT. The second approach evaluates each pulse or range-bin and tunes the FRFT order for the optimal response. This is referred to as the local optimization procedure (LOP) [2, 34]. While the first global optimization approach is easier to implement and provides improved results, the finely tuned LOP provides the best performance [34]. Figure 5.7 shows the FRFT modified CSA which includes a pre-azimuth FRFT filter to correct for mismatches between the received pulses and the range FM rate K_r, and a modification of the azimuth match filter to maximize contrast for each range-bin using the FRFT to optimize the azimuth FM rate K_a. Note that, for the LOP approach, the FRFT optimization values need to be obtained using some approach; the approach we adopt in this work is discussed in the next section. Note also that the forward and inverse FRFTs are not optimized. The FRFT order is set to $\kappa = 1$ so the FRFT is the classical FT. This was done to provide easy modification of the new CSA procedure and allow for direct comparison to the CSA in Figure 2.2 without transform optimization.

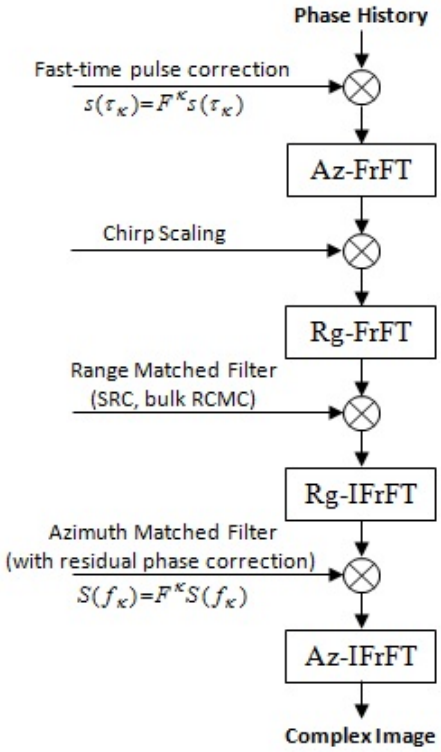

Figure 5.7: Block diagram providing an overview of fractional focusing with CSA.

Figure 5.7 is a block diagram overview of the fractional CSA. The Rg-FrFT indicates that the FRFT is applied in the range direction, and the Az-FrFT indicates that the FRFT is applied in the azimuth direction. The IFrFTs indicate the inverse transform provided with the inverse FRFT property $(F_r^\kappa)^{-1} = F_r^{(-\kappa)}$. Secondary range compression and range cell migration correction (RCMC) are applied in the range matched filtering step. Differential RCMC is applied in the chirp scaling step.

The fractional CSA begins with a 2-D array of demodulated raw (unprocessed) phase-history data $s_r(t,\eta)$ as given in Equation (2.2). The phase-history data is in the range-time and azimuth-time domains, respectively indicated by t and η.

The fractional focusing CSA steps [1, 2] are summarized as follows[1],

1. The fractional filter is applied to each received pulse,
   $s_r(t_\kappa,\eta) = (F_r^\kappa s_r)(t_\kappa,\eta)$. Since this is only applied to the fast-time pulses, the

range-time variable t is updated to t_κ, indicating that the TF plane of the signal is rotated by κ.

2. An azimuth FRFT is performed to transform the data into the range Doppler domain,
   $S_{rd}(t_\kappa, f_\eta) = (F_r^1 s_r)(t_\kappa, \eta)$. With the FRFT order set to 1, the data is transformed to the range-time, azimuth-frequency domain, also referred to as the range Doppler domain; this is indicated by the change of η to f_η. Since this is equivalent to applying the classical FT, the azimuth frequency index is not affected.

3. Chirp scaling is applied, using a phase multiply to equalize the range migration of all targets, $S_1(t_\kappa, f_\eta) = s_{sc}(t, f_\eta) S_{rd}(t_\kappa, f_\eta)$.

4. A range FRFT is computed to transform the data to the 2-D frequency domain,
   $S_2(f_{t_\kappa}, f_\eta) = (F_r^1 S_1)(t_\kappa, f_\eta)$. The range-time variable t_κ is updated to indicate range-frequency f_{t_κ} with no additional fractional rotations.

5. A phase multiply is performed with a reference function, which applies range compression, SRC, and bulk RCMC in the same operation,
   $S_3(f_{t_\kappa}, f_\eta) = S_{MF_{Range}}(f_t, f_\eta) S_2(f_{t_\kappa}, f_\eta)$.

6. A range IFRFT is performed to transform the data back to the range Doppler domain, $S_4(t_\kappa, f_\eta) = (F_r^{-1} S_3)(f_{t_\kappa}, f_\eta)$. The range Doppler is indicated with t_κ, f_η.

7. A phase multiply is performed to apply azimuth compression with a time varying match filter. A phase correction is also required as a result of the chirp scaling in step 2, which is incorporated into the same phase multiply,
   $S_5(t_\kappa, f_{\eta_\beta}) = (F_r^\beta S_{MF_{Azimuth}})(t_\kappa, f_{\eta_\beta}) S_4(t_\kappa, f_{\eta_\beta})$. Contrast maximization is achieved by applying F_r^β in the azimuth direction. The new azimuth-frequency variable is updated to f_{η_β}, indicating that the TF plane of the azimuth signal is rotated by β.

8. The final azimuth IFRFT is performed to transform the compressed data to the SAR image domain, $S_6(t_\kappa, \eta_\beta) = (F_r^{-1} S_5)(t_\kappa, f_{\eta_\beta})$. The data is now back in the range-time, azimuth-time domains, with FRFT optimizations indicated by the updated variables t_κ, η_β. Also, since this is the last step, the data is compressed in both range and azimuth. This ensures that the data is suitable for additional processing or detected and scaled for image display.

[1]The subscripts κ, β on the index variables, indicate that the TF plane for the signal data is in the fractional domain or the data along that axis is rotated by a fractional operator $\alpha \neq n\pi, n \in \mathbb{N}$, or $\alpha = (\pi/2)n, n \in \mathbb{N}$ for $\alpha = \kappa\pi/2$ or $\alpha = \beta\pi/2$.

CHAPTER 6

Application of Enhanced FRFT Focusing Technique Using RADARSAT Data

In Chapter 5, we presented the enhanced fractional Fourier transform (FRFT) technique based on enhancements of the chirp scaling algorithm (CSA). This fractional focusing method is a first attempt at implementing the fractional CSA (FrCSA) provided in [2]. It includes modifications that were necessitated by the use of the fractional autocorrelation function (FrACF) to obtain locally optimized FRFT rotational parameters from real SAR images. In this chapter, we apply the enhanced FRFT focusing (EFrF) technique to SAR data obtained from RADARSAT scenes.

We will obtain performance comparisons between the standard CSA and the EFrF implementation by setting the FRFT order $\kappa = 1$ for the original CSA steps requiring fast Fourier transforms (FFTs). A challenge that has not been addressed with this implementation is the generation of the optimal FRFT transform parameters. We will present one approach; however, given the additivity of the rotations property of the FRFT $F_r^{\kappa 1+\kappa 2} = F_r^{\kappa 1} F_r^{\kappa 2}$, and the time-frequency plane, many optimized fractional CSA implementations are possible by combining standard SAR signal processing techniques with the FRFT to obtain optimal transform parameters.

We will first describe the test environment, followed by the generation of the optimized transform parameters for a RADARSAT-1 [41, 42] scene, then provide results of our fractional CSA implementation.

6.1 Processing Architecture

All processing in this thesis was accomplished on a Sun Ultra24 Workstation (Quad x86) with the following configuration: (a) Operating System: SunOS 5.11; (b) Compiler:

Sun Studio 12; (c) Programming Language: FORTRAN 90; (d) Parallel Processing: Open Multi-Processing (OpenMP); (e) All FFTs: Sun Performance Library (ZFFTZ); and (f) Polynomial regression: Netlib (DGETRF, DGETRI)

6.1.1 FRFT Algorithm Implementation

To enable FRFT processing on the above architecture, it was necessary to port the MATLAB *fracF* routine in Section 3.3.1 to FORTRAN 90. It could have also been ported to C or C++ but we wanted to work with FORTRAN since all the high performance algorithm libraries are written in FORTRAN. Sufficient testing was conducted to verify that the ported FORTRAN module provided the same results as the MATLAB *fracF* routine. Testing consisted of comparing both the real and imagery parts of a rectangular function processed at FRFT orders between 0.5 and 1.0.

The *fracF* is considered $O(N\log_2 N)$ where N is the number of data samples, however its implementation compared to the FFT was noticeably slower. In addition to the two chirp multiplications and the frequency domain multiplication to accomplish the convolution, the *fracF* algorithm required two FFTs of length $2N$ and three FFTs of length $16N$. Since all of the filter and data arrays are $N = 4096$ or radix-2, an approximation of the complexity is $4N\log_2 2N + 48N\log_2 16N$ which is approximately 68 times higher than $N\log_2 N$ for the standard FFT.

A comparison of performance on the test architecture was performed using a one dimensional (1-D) FFT on the 4096x4096 data array. The test was accomplish using a single thread that the standard FFT completed in 0.97 seconds and the *fracF* procedure completed in 88.38 seconds, which is still considerably faster than an implementation of complexity $O(N^2)$.

6.2 RADARSAT-1 Scene Phase History Data

The RADARSAT-1 phase-history data was included with the book *digital processing of Synthetic Aperture Radar Data* [1] and made available by Gordon Staples of Radarsat International. The Canadian Space Agency holds the copyright, and it is provided on condition that it only be used for educational purposes.

The data is provided in CEOS format, and MATLAB routines are made available for extracting the CEOS format data from the CD. The MATLAB routines also make necessary corrections to account for fluctuations in the gain or automatic gain control (AGC) during the collect.

Some of the RADARSAT-1 scene parameters are listed below. To account for the minimum array size needed for convolution, good FFT sizes and minimum number of samples to meet compact signal support requirements, all arrays with be over-sampled (zero padded) to a length 4096. The raw phase-history samples used as input to the CSA were 2048x2048, or 2048 pulses by 2048 range-bins. Due to interpolation methods used in the *fracF* routine, all phase-history data and matched filters were symmetrically zero padded keeping the original data in the center of the up-sampled arrays. Table 6.1 contains some RADARSAT-1 non-changing parameters that are used in the matched filter and chirp scaling operations.

Table 6.1: RADARSAT-1 Fine-beam:2 parameters

Parameter	Symbol	Value	Units
Sampling rate	f_s	32.317	MHz
Pulse bandwidth		30.11	MHz
Range FM rate	K_r	721.35	GHz/s
Pulse duration	T_r	41.74	μs
Number of range samples	N_r	1349	samples
Center frequency	f_0	5.30	GHz
Wavelength	λ	0.05657	m
Pulse repetition frequency	PRF	1256.98	Hz

The actual Vancouver scene is a small subset of an overall larger scene of phase-history data provided in [1]. Table 6.2 contains a list of parameters that change throughout the scene based on either range or time.

Table 6.2: RADARSAT-1 Vancouver scene parameters

Parameter	Symbol	Value	Units
Slant range (scene center)	R_0	974804	m
Effective radar velocity	V_r	7052.2	m/s
Doppler centroid	f_{η_c}	-8190	Hz
Azimuth FM rate	K_a	1795	Hz/s
Number of azimuth samples	N_a	705	samples

6.3 FM Rate Estimation Using Fractional Autocorrelation and Contrast Maximization

In Section 4, we characterized the performance of the fractional autocorrelation function (FrACF) detector against the Cramér-Rao lower bound (CRLB) in varying signal-to-noise ratio (SNR) environments. To provide a measure of FrACF performance using the received RADARSAT-1 data, we will need to provide an estimate of the received and processed SNR. The SNR of a SAR signal is governed by the radar range equation and, for an uncompressed pulse it is given by [1, 6, 43, 3],

$$\mathrm{SNR}_{image} = \frac{P_{av} G^2 \lambda^2 \sigma}{(4\pi)^3 R^3 k T_o B L V \rho_a} \tag{6.1}$$

where P_{av} is the average power, G is the antenna gain, σ is the target radar cross section (RCS), R is the slant range, k is Boltzmann's constant, T_o is 290 degrees Kelvin, B is the receiver bandwidth, L is radar losses, ρ_a is the azimuth resolution and V is the platform velocity. If clutter is being observed, then $\sigma = \sigma_0 \rho_a \rho_r / \cos\psi$, providing the clutter-to-noise ratio (CNR) as

$$\mathrm{CNR} = \frac{P_{av} G^2 \lambda^3 \sigma_0 \rho_r}{2(4\pi)^3 R_k^3 k T_o B L V \cos\psi} \tag{6.2}$$

where σ_0 is the backscatter coefficient, ψ is the grazing angle and ρ_r is the range resolution. Since we are working with previously collected data and the randomness of σ_0 in (6.2), it will be necessary to obtain an CNR estimate based on SAR imagery (speckle) noise components.

The total noise in SAR imagery σ_N, is comprised of two components, additive noise σ_n which is the result of thermal noise and multiplicative which is the signal dependent noise proportional to the average signal level $\bar{\sigma}_0$ [6],

$$\sigma_N = \sigma_n + (\mathrm{MNR})\bar{\sigma}_0 \tag{6.3}$$

where MNR is the multiplicative noise ratio, and the relationship of σ_n to CNR is

$$\sigma_n = \sigma_0/\text{CNR}. \tag{6.4}$$

The principle contributors of MNR are the integrated sidelobe ratio (ISLR) of points in the surrounding area, ambiguities in the image, quantization noise and image artifacts or MNR = ISLR + QNR + AMBR, where QNR is the quantization ratio and AMBR is the ambiguity ratio [6]. Figure 6.1 is a plot of image clutter for $|\text{MNR}| < |\text{CNR}|$ showing the effect of MNR on the ISLR of points used to produce the image clutter. As noted, MNR is the ratio of the image no-return area (NRA), divided by the average image clutter [3]. Note that the total noise in the NRA is $\sigma_{N_{NRA}} = \sigma_n + (\text{QNR} + \text{AMBR})\bar{\sigma}_0$.

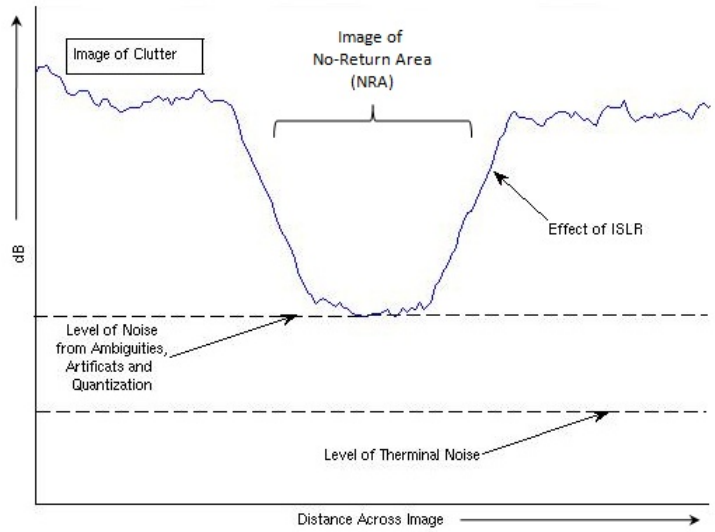

Figure 6.1: Plot of image clutter for $|\text{MNR}| < |\text{CNR}|$, showing the relationship of total noise σ_N with the total noise in the NRA, $\sigma_{N_{NRA}}$. A similar graphic is provided in [3].

Since the LFM detection simulations assumed an additive noise model, we will use the ratio of the total noise in the NRA with the total of the image clutter for CNR estimates used to gauge detection performance. One reason for this approach is that, $\sigma_{N_{NRA}}$ can be estimated directly form the received or processed data. Since this involves MNR, we must

address limitations of time-frequency (TF) LFM chirp rate detection methods for signals with MNR > 1. Results of simulations in [44] indicate the instantaneous frequency (IF) of signals corrupted with both multiplicative and complex additive white Gaussian noise (AWGN), is that the IF estimation can be accomplished with time frequency methods provided the standard deviation of the multiplicative noise is less than its mean. It is noted in [45] that the MNR is the ratio of the standard deviation over the mean and that the theoretical MNR of a single look amplitude SAR image is 0.5227. Since this is less than 1.0, time frequency methods such as the FrACF can be used to estimate the IF or LFM chirp rates.

The method that will be used to provide an estimate of the noise will be to identify regions in the collected or processed imagery where there is little or no back-scatter energy such as radar shadows or large areas of calm water [6, 3, 45]. Since the multiplicative noise component is proportional to the average signal level $\bar{\sigma}_0$, the CNR will be estimated as the ratio of the NRA to total image clutter. Figure 6.2 is the magnitude of received phase-history data from RADARSAT-1 suitable for processing into a SAR map (image). For this data, range is increasing from left to right and the satellite was moving from top to bottom, transmitting and receiving pulses at the pulse repetition frequency (PRF). Each received pulse is sampled at 32.317 MHz providing a 2-D array of phase-history data. The received baseband signal data is given by (2.2). To provide a comparison of detector performance in varying CNR regions, we will obtain the CNR in dB using,

$$\text{CNR}_{dB} = 10\log_{10}\left(\frac{P_{signal}}{P_{noise}}\right) \tag{6.5}$$

where P_{noise} will be chosen from homogeneous regions in both the phase history data sets depicted in Figure 6.2 and Figure 6.5 [6, 3, 45]. Since the homogeneous regions and received pulses will not be the same length, (6.5) can be redefined as,

$$\text{CNR}_{dB} = 10\log_{10}\left(\frac{E\{|s-\sigma_{N_{NRA}}|\}^2}{E\{|\sigma_{N_{NRA}}|\}^2}\right) \tag{6.6}$$

where s is a 1-D array containing the pulse or range-bin samples and $E(\cdot)$ is statistical expectation.

The detection was done with FrACF and the performance is provided in Figure 6.3 which is in agreement with the results of the simulations in that, the performance of FrACF will depend on having good SNR. Both detection and CNR calculations can be noisy so a smoothing filter was used when necessary to help identify trends in the plotted data. When a smoothing filter was used, this was indicated on the plot as $win(n)$ where n is the length of the filter used in the MATLAB convolution (*conv*) routine.

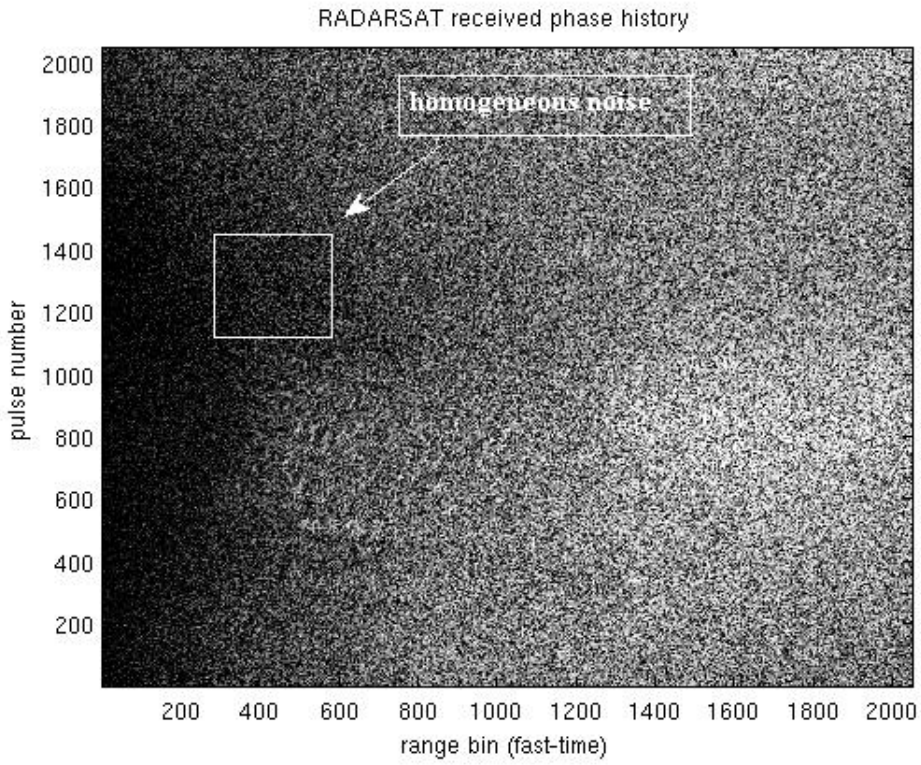

Figure 6.2: RADARSAT-1 phase-history data (Vancouver Airport BC).

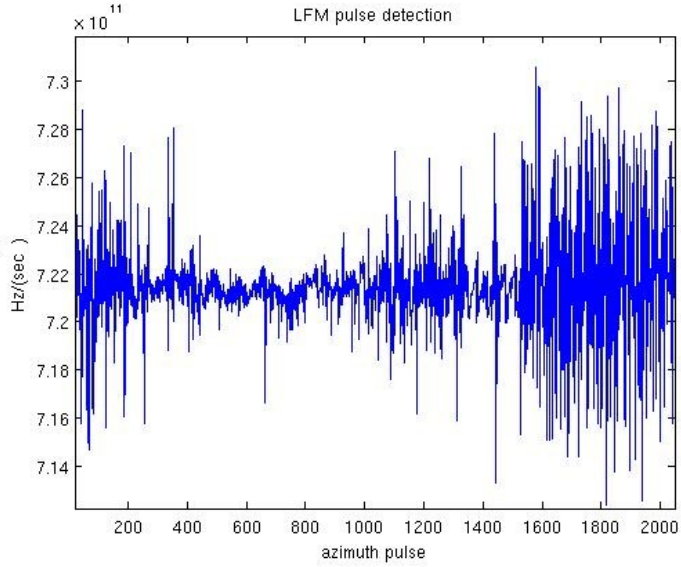

Figure 6.3: Range FM rate detection using FrACF.

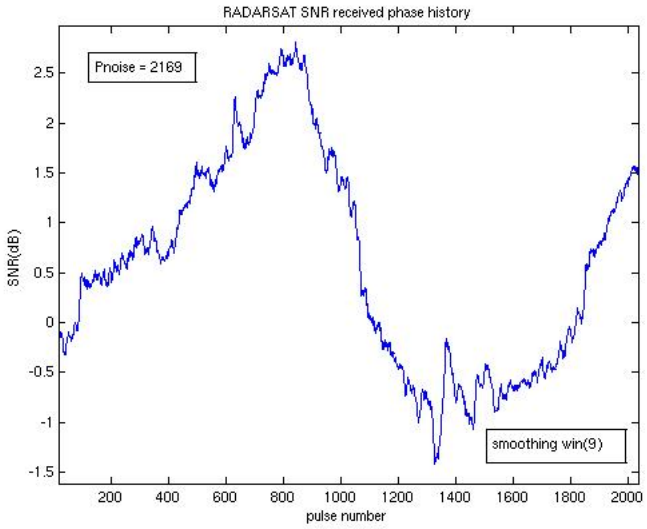

Figure 6.4: Range SNR for RADARSAT-1 scene (Vancouver Airport BC).

Figure 6.5 is an image of the phase-history data in the range Doppler domain, after range pulse compression (matched filtering) and range cell migration correction (RCMC) and the data in this domain is provided by Equation (2.20).

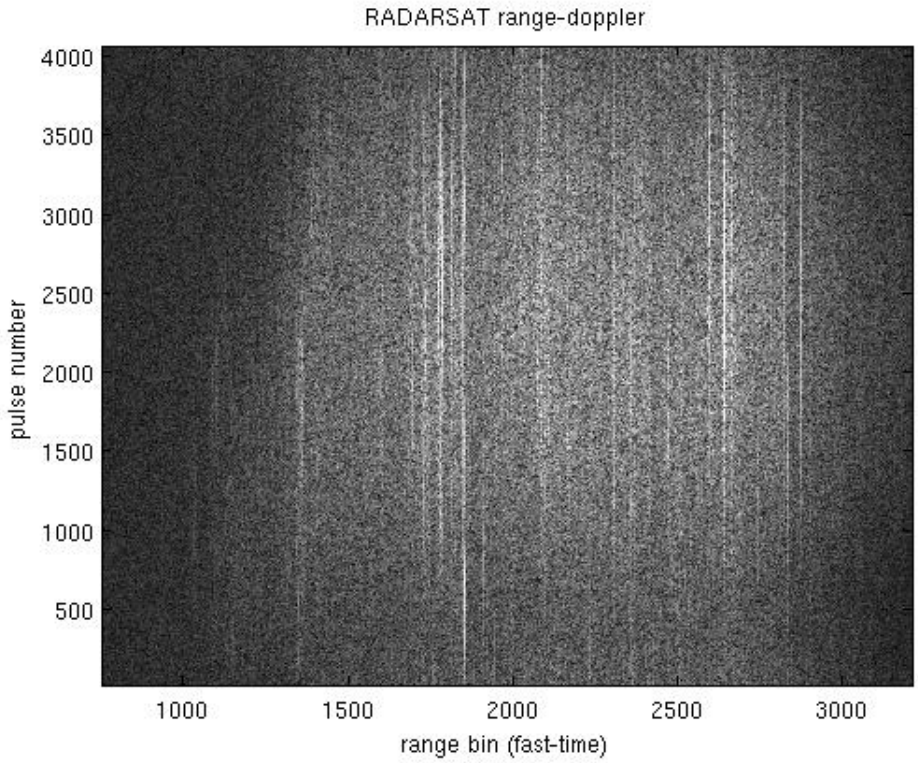

Figure 6.5: RADARSAT-1 range Doppler (Vancouver Airport BC).

We see in Figure 6.6 that the azimuth LFM rate detector performed well mainly due to good CNR in the range Doppler domain after range compression and range cell migration correction.

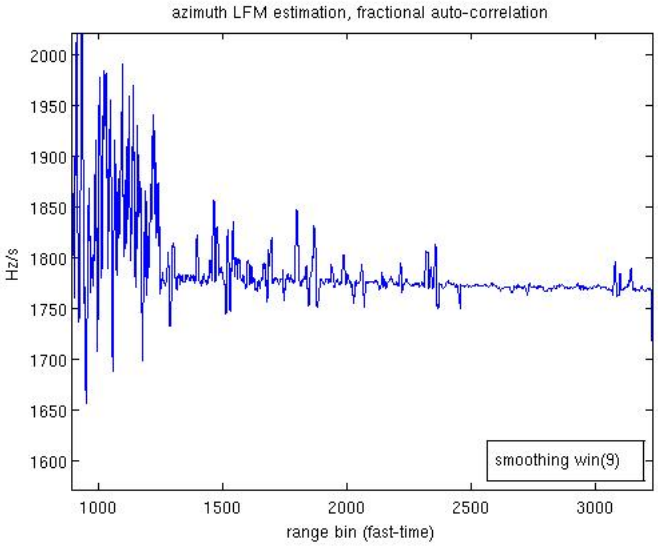

Figure 6.6: Azimuth FM rate detection using the FrACF.

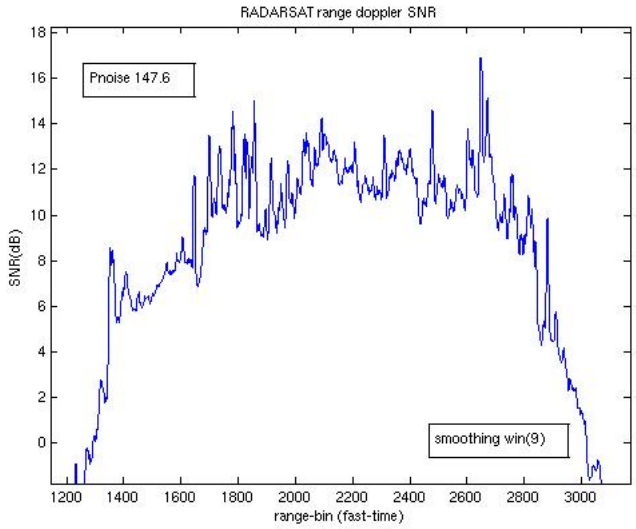

Figure 6.7: Azimuth CNR for RADARSAT-1 scene.

Comparing the range and azimuth FM rate detection performance in Figure 6.3 and Figure 6.6, we can see that the azimuth FM rate detection performed better in that there is less noise and an overall trend noticeable in Figure 6.6, whereas in Figure 6.3 we notice possible good LFM detection in the region where the CNR peaked between pulse

numbers 400 - 1000. The better estimation performance of the azimuth detector can be attributed to performing the detection on the data in the range Doppler domain after range compression. Since it is after range compression, the CNR is improved as indicated in Figure 6.7. It should also be noted, that clear SAR imagery is dependent on having CNR between 5 dB and 15 dB [3] and this threshold is evident in Figure 6.7.

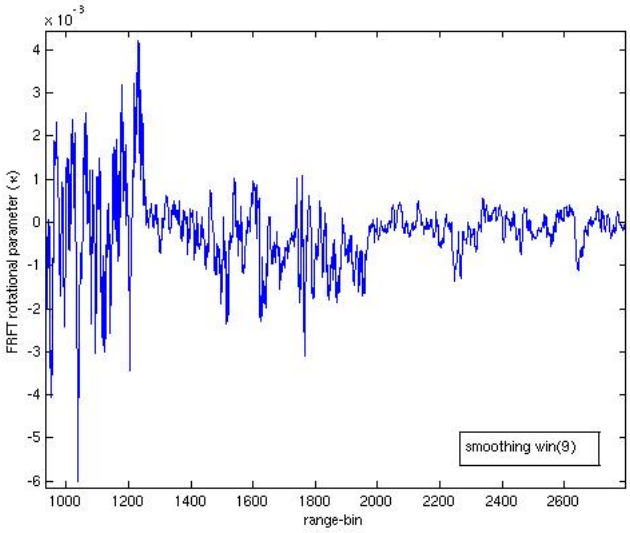

Figure 6.8: Azimuth FRFT optimized parameters using contrast maximization.

Figure 6.8 is a plot of the optimized FRFT rotational parameters using contrast maximization for the detection statistic in (4.11). Since this statistic is captured during the azimuth matched filtering stage, the target energy is fully compressed. For this implementation, the algorithm maximizes the contrast of the strongest target within each range bin. It is also possible to force the maximization for specific spatial regions by bounding the regions for which contrast is maximized. Both MATLAB and FORTRAN provided intrinsic routines for selecting maximum values and their locations in multi-dimensional arrays.

To obtain a better estimate for the range FM rate, we performed the detection after azimuth compression when the CNR is improved and, as expected, this did provide a better noise estimate. Figure 6.9 is a plot of the CNR for each pulse using Equation (6.6)

on data that is compressed in both range an azimuth, in other words, a single look complex (SLC) image. As shown in Figure 6.10, the CNR is well above the needed threshold of 5 dB as indicated in Figure 4.2. Figure 6.10 is a plot of the FRFT optimization values κ obtained using FrACF.

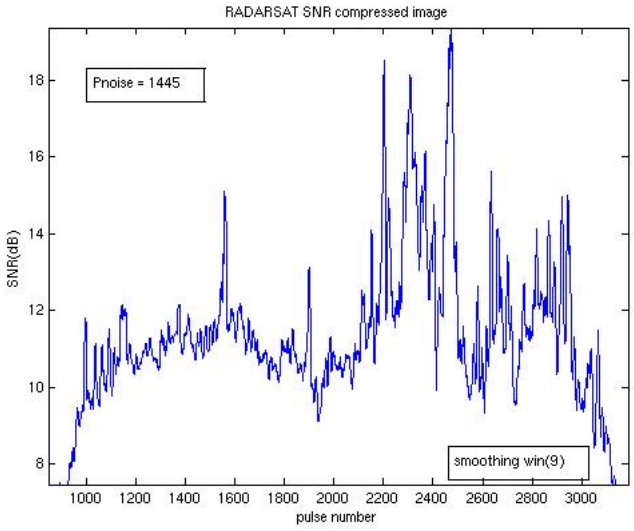

Figure 6.9: Clutter-to-noise (CNR) ratio for each pulse from a single look complex (SLC) image (compressed in both range and azimuth).

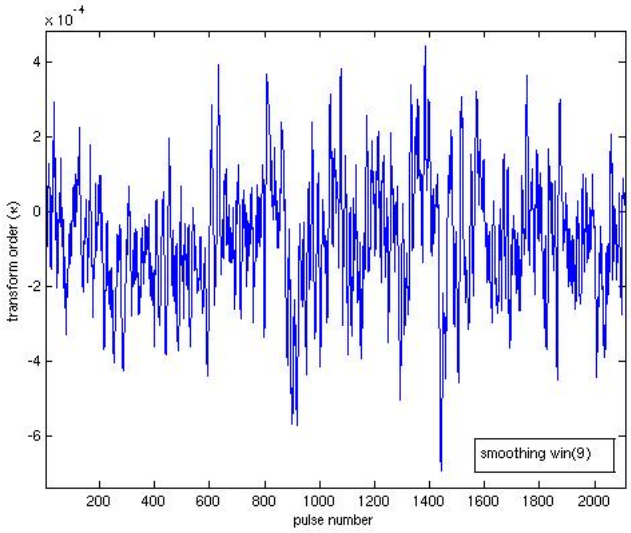

Figure 6.10: Pulse FRFT optimization values obtained using the FrACF.

Using the noisy estimates to correct mismatches in the range FM rate caused severe streaking or high noise levels in the azimuth direction of the SLC image. Since we are using the FRFT to correct for nonlinear motion between the satellite and target, it is not possible for the uncompensated motion to change this rapidly for non-moving targets, so the range FM estimates were used as input to a polynomial fitting algorithm. The fitted polynomial will be used for the pulse FRFT optimization values and a plot of the values is provided in Figure 6.8. Note that FRFT optimization values are the difference between the matched filter and received data LFM chirp rates, and are corrections to the azimuth dependent range FM rates needed to concentrate the frequency in the TF plane as demonstrated in Figure 5.3. These corrections are provided as updates to the original FM rate using the FRFT operator additivity property.

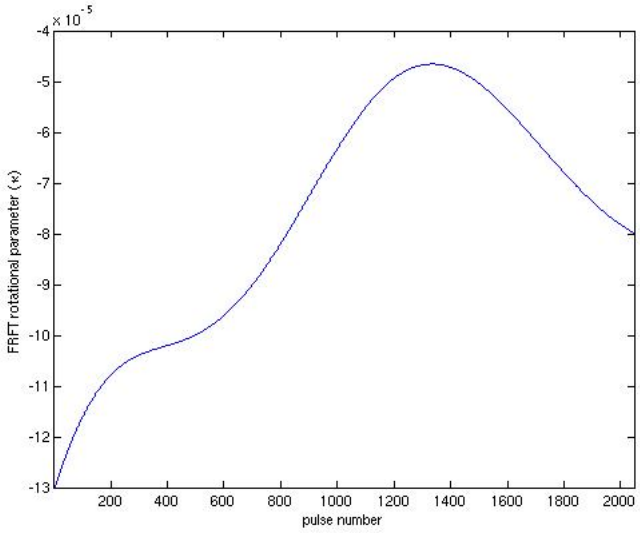

Figure 6.11: Pulse FRFT optimization values using FrACF; for $\kappa = -7e^{-5}, \Delta K_r = -2.8e^{8}$ using Equation (4.19).

6.4 Fractional Auto Focus for Chirp Scaling Algorithm

The fractional focusing CSA was implemented using the steps depicted in the overview Figure 5.7.

6.4.1 Fast-time FRFT chirp optimization

The first FRFT optimization was applied to each pulse using the values in Figure 6.11, $s_r(t_\kappa, \eta) = (F_r^\kappa s_r)(t_\kappa, \eta)$. This is done by applying a 1-D FRFT to each row of $s_r(t_\kappa, \eta)$ with $\kappa_i = \text{FRFT}_{order}(i)$.

6.4.2 Azimuth FRFT

A azimuth FRFT is performed by applying a 1-D FRFT to each column or range-bin with $\kappa_i = 1$ for all range-bins, $S_{rd}(t_\kappa, f_\eta) = (F_r^1 s_r)(t_\kappa, \eta)$. Notice the frequency index f_η

indicating the data is now in the range-time azimuth-frequency domain.

6.4.3 Chirp scaling

Chirp scaling is applied using the f_η dependent phase multiply, $S_1(t_\kappa, f_\eta) = s_{sc}(t, f_\eta) S_{rd}(t_\kappa, f_\eta)$. This is accomplished with a 1-D multiply applied to each row of the 2-D data array. The phase multiply is provided with (2.16).

6.4.4 Range FRFT

A range FRFT is performed by applying a 1-D FRFT to each row or pulse with $\kappa_i = 1$ for all pulses, $S_2(f_{t_\kappa}, f_\eta) = (F_r^1 S_1)(t_\kappa, f_\eta)$. The phase-history data is now in the 2-D frequency domain. The frequency indexes f_{t_κ} and f_η indicate the data is now in the range-frequency, azimuth-frequency domain.

6.4.5 Range matched filter

An f_η dependent range matched filter is applied to remove the second and forth exponential terms of (2.18), $S_3(f_{t_\kappa}, f_\eta) = S_{MF_R} S_2(f_{t_\kappa}, f_\eta)$. The phase of matched filter is,

$$\phi_{RangeMF} = \frac{\pi D(f_\eta, V_r)}{K_m D(f_{\eta_{ref}}, V_r)} f_t^2 + \frac{4\pi}{c} \left[\frac{1}{D(f_\eta, V_{r_{ref}})} - \frac{1}{D(f_{\eta_{ref}}, V_{r_{ref}})} \right] R_{ref} f_t \qquad (6.7)$$

A 1-D range matched filter if applied by multiplying each row of the $S_2(f_{t_\kappa}, f_\eta)$ with $F_r^1 \left\{ \exp(j\phi_{RangeMF}) \right\}$.

Figure 6.12 is a plot of the phase and matched filter for pulse 2048.

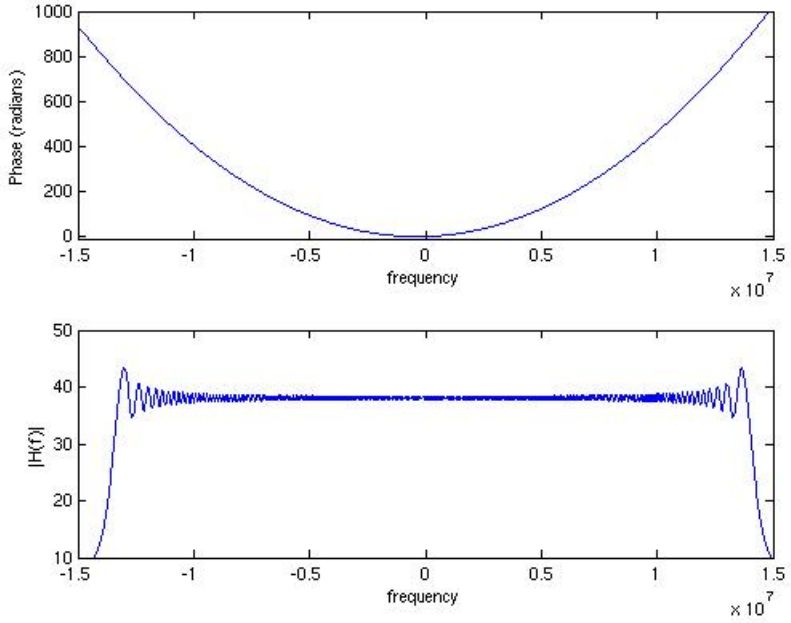

Figure 6.12: Range matched filter phase and magnitude for pulse 2048.

6.4.6 Range IFRFT

A range IFRFT is performed by applying a 1-D FRFT to each row or pulse with $\kappa_i = -1.0$ for all pulses, $S_4(t_\kappa, f_\eta) = (F_r^{-1} S_3)(f_{t_\kappa}, f_\eta)$. The phase-history data is now in the range Doppler domain.

6.4.7 Azimuth matched filter

A t_κ dependent azimuth matched filter is applied to remove the first term of (2.18) and (2.25), $S_5(t_\kappa, f_{\eta_\beta}) = (F_r^{\beta} S_{MF_{Az}} S_4)(t_\kappa, f_{\eta_\beta})$. The phase of matched filter is,

$$\begin{aligned}\phi_{AzimuthMF} =& \frac{4\pi R_0 f_0 D(f_\eta, V_r)}{c} \\ &+ \frac{4}{c^2}\frac{\pi K_m g_1}{\pi K_m + g_1}\left[\frac{R_0}{D(f_\eta, V_r)} - \frac{R_{ref}}{D(f_\eta, V_{r_{ref}})} + \frac{c g_0}{4 g_1}\right]^2 + \frac{g_0^2}{4 g_1}\end{aligned} \tag{6.8}$$

With the application of the matched filter, the FRFT optimization is applied to maximize contrast using the optimization values displayed in Figure 6.8. The FRFT optimized 1-D

matched filter is applied to each column of $S_4(t_\kappa, f_\eta)$ using, $F_r^{\beta_i}\{\exp(j\phi_{AzimuthMF})\}$. The Netlib algorithms DGETRF and DGETRI were used as a polynomial fitting routine to produce the coefficients g_0 and g_1.

6.4.8 Azimuth IFRFT

A azimuth IFRFT is performed by applying a 1-D FRFT to each column or range-bin with $\kappa_i = -1.0$ for all range-bins, $S_6(t_\kappa, \eta_\beta) = (F_r^{-1}S_5)(t_\kappa, f_\eta)$. The data is now compressed in both range and azimuth with concentrated target energy. This product is often referred to as a single look complex (SLC) image.

6.4.9 Results

The result of the CSA or fractional focusing CSA is an single look complex (SLC) image. Each pixel of this image has an I and Q or real and imaginary component and often, the dynamic range of the magnitude $y(m,n) = \sqrt{I(m,n)^2 + Q(m,n)^2}$ exceeds the display capabilities of common display systems. There are many algorithms and theories for remapping the pixels into an acceptable display range, many of which make use of log functions and image statistics. The remap of the SLC image included was accomplished using a nonlinear contrast stretch routine that remapped all pixel values between the minimum and maximum magnitude $\left(\sqrt{I^2 + Q^2}\right)$ values to an 8-bit display range of 0 to 255. Also, it is customary to project the slant plane SLC image into the ground plane before remapping. This slant-to-ground projection was not performed, hence the image is in the slant plane.

An overview image (1/8 resolution) is provided in Figure 6.13, where azimuth-time is increasing from the bottom to top and range increases from let to right.

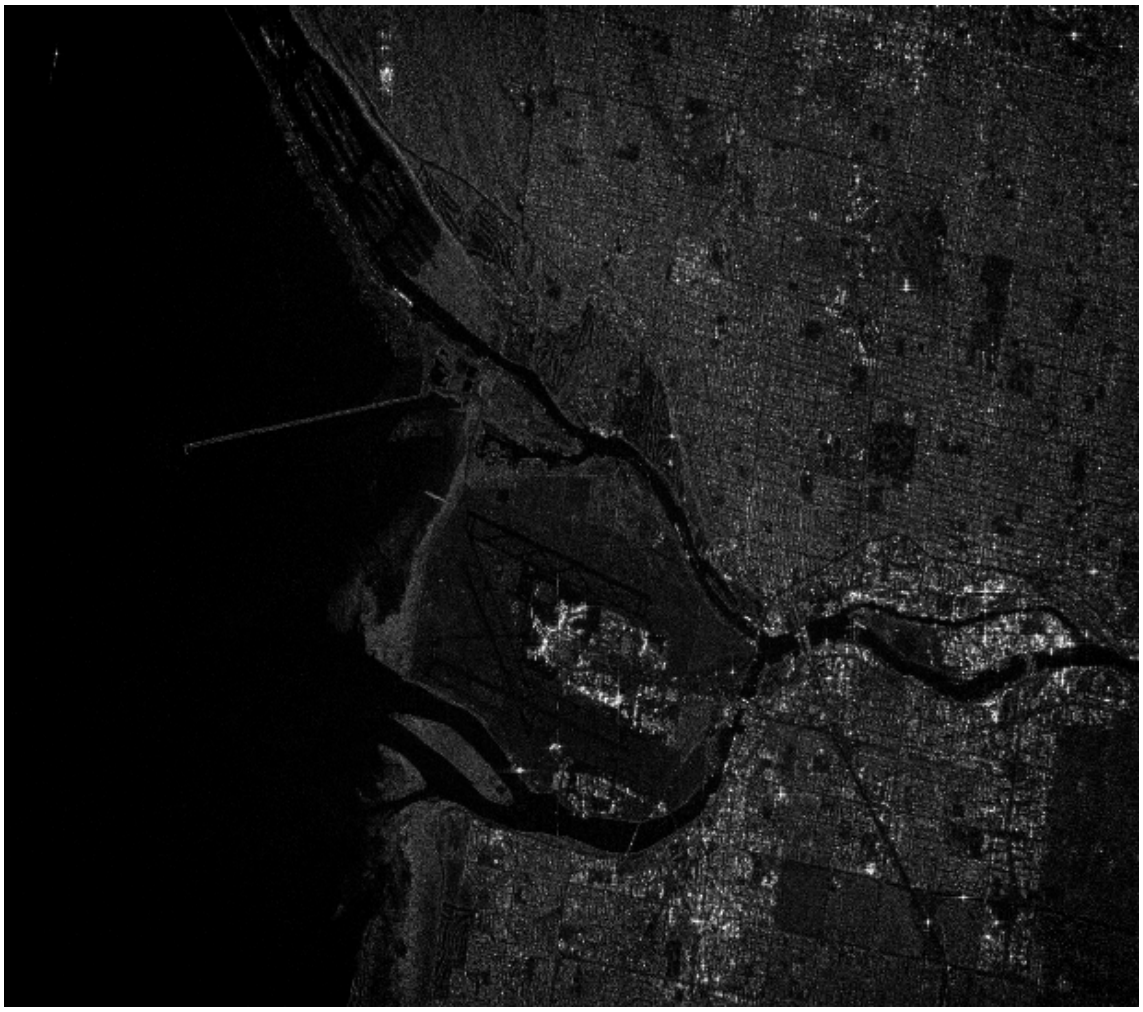

Figure 6.13: RADARSAT-1 scene (Vancouver, BC).

Figure 6.14 is a full resolution chip from the center of the RADARSAT-1 scene used for this evaluation. First to get an appreciation of what 8 meter resolution imagery looks like, the runway 08L-26R marker was placed in the chip. According to the Vancouver airport guide, that runway is 200 feet wide. Since we will be comparing performance enhancements of the FRFT, no attempt was made to improve the overall response by including weighting functions or multi-look methods in the processing (this is mentioned because weighting functions such as the Taylor window are standard techniques used in SAR signal processing for mitigating side-lobe levels.) There are two rectangles placed

around areas of bright return to indicate regions for calculating contrast. See Table 6.3 for contrast values. EFrF is used to indicate fractional focusing in the CSA. The area Loc (1) is the rectangle in the upper region of the chip (approximate row 2250) and Loc (2) is the lower region (approximate row 2450). Also included in the table is a point target located at row 2634, column 1967. This target is not located within the full resolution chip but is noticeable in the 1/8 resolution scene.

Table 6.3: RADARSAT-1 Vancouver scene contrast comparisons

Location	CSA	FFrF
Loc (1)	3.797	4.013
Loc (2)	4.829	5.109
(2634,1967)	3.004	3.113

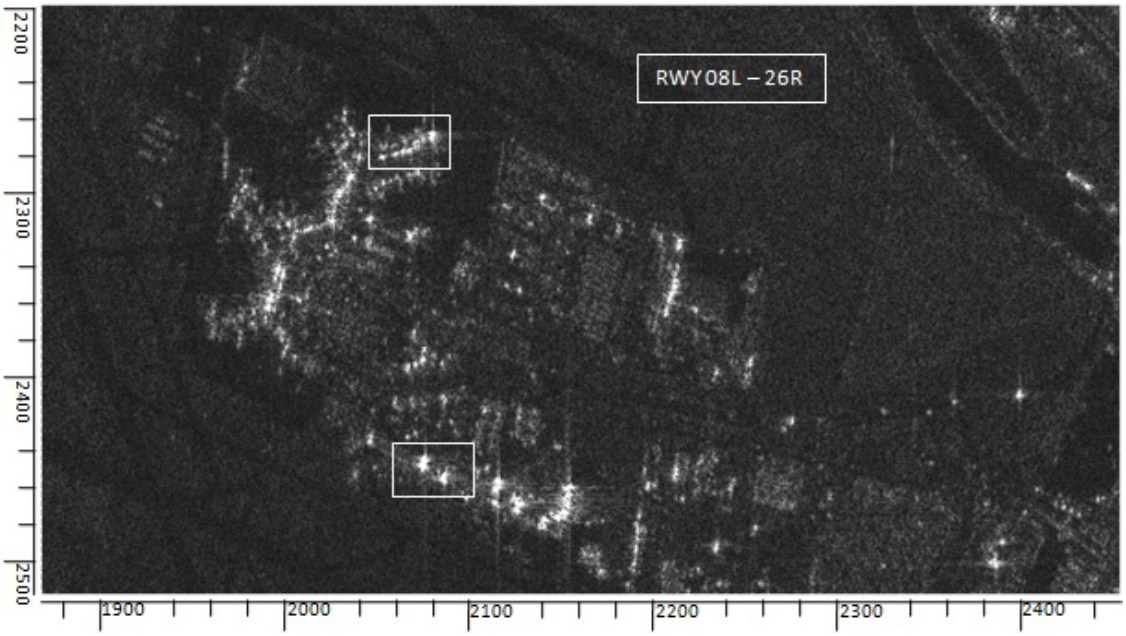

Figure 6.14: Full resolution chip of the RADARSAT-1 scene.

Figure 6.15 is a point target located at row 2424 column 2415. To produce the MATLAB plots, the complex points are up-sampled by a factor of 16. The target on the left is from CSA processing with original FT or FRFT order F_r^1. The target on the right was

produced using the same algorithm and parameters except that the FRFT LOP parameters or F_r^K applied as indicated in Figure 5.7. We see a significant improvement in the range direction especially in the resolution; this is a result of correcting the FM rate mismatch. In other words, the target is no longer walking across range bins but aligned in frequency or time as depicted in Figure 5.3.

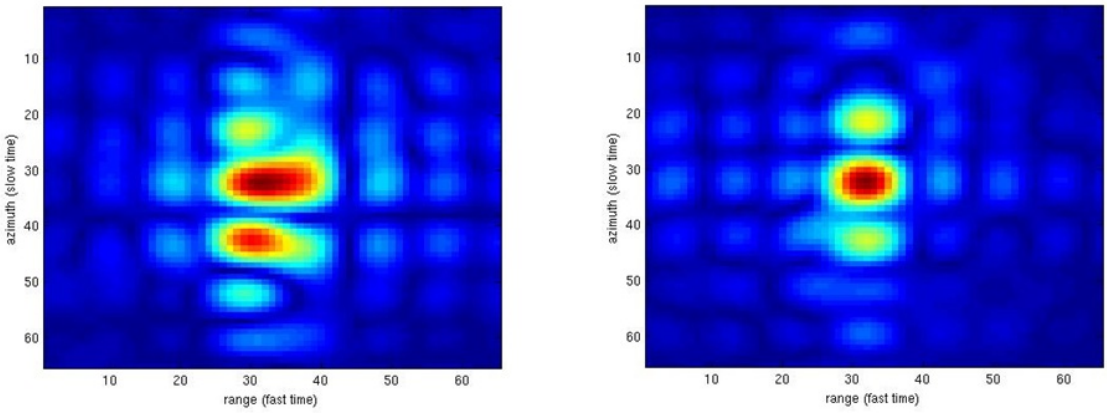

Figure 6.15: MATLAB point target analysis at target location (2424,2415). Target upsampled by a factor on 16 and displayed with MATLAB routine *imagesc*.

Figure 6.16 provides a fast time comparison of point target at row 2424. For this target it is easy to see an improved peak sidelobe ratio (PSLR) (approximately 1dB) along with an overall improvement in the impulse response width (IRW) or resolution. It should be noted, that it is customary to provide comparisons in dB, however we wanted to keep the scaling between Figure 6.15 and Figure 6.16 comparable.

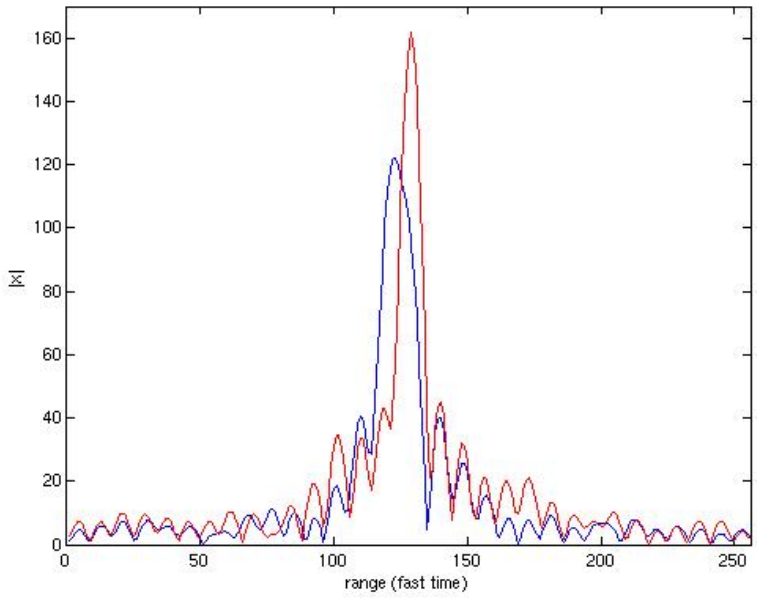

Figure 6.16: Point target fast-time comparison (azimuth pulse 2424).

CHAPTER 7

Conclusions and Future Work

7.1 LFM Detection Accuracy

From both the high resolution results presented in [16] and our simulation-error analysis results, we can conclude that fractional autocorrelation function (FrCSA) is an efficient method for LFM detection with high performance in low SNR environments. For RADARSAT-1 LFM chirp rate estimation, Figures 4.2 and 4.4 indicate that FrACF can be used for estimation in SNR environments above 5 dB. One measure of SAR image quality is quadratic phase error (QPE) which contributes to elevated sidelobe and broadening of the impulse response width (IRW). A mismatch of FM rates between the matched filter and returned signal will contribute to QPE thereby decreasing image quality. A rule of thumb for high focusing [1] accuracy (less than 2 percent IRW boarding), is

$$\left|\frac{\Delta K}{K}\right| \leq \frac{1}{\text{TBP}} \tag{7.1}$$

where K is the FM rate, $\Delta K$is the FM rate mismatch and TBP is the time bandwidth product. This indicates that the range FM rate mismatch must be, $\Delta K_r \leq 0.57$ GHz/s and the standard deviation in Figure 4.3 indicates that this can be achieved in normal SNR environments.

The detection performance for the RADARSAT-1 scene in Figures 6.3 and 6.6 are in agreement with the MSE simulations indicating that the FrACF can be used for FM rate detection in good SNR environments. One possible approach to enhance the detection of the range FM rate could be to perform the detection after azimuth compression to enhance the SNR of each pulse. Depending on how this is implemented, it could result in performing complete image formation processing twice.

7.2 Fractional Focusing and the CSA Implementation

While the concentration of this work has been the use of the FRFT to enhance the focusing of the CSA, some of the obtained results require additional consideration.

7.2.1 Contrast Maximization

The results of testing contrast maximization with changing FM rate K_a and changing FRFT order κ indicate that the FRFT has the capability to enhance the contrast beyond that of correcting the FM rate mismatch. This is depicted in Figure 5.6 and suggests that matched filtering at optimal FRFT orders will increase the peak sidelobe ratio (PSLR) compared to classical FT methods. The expected behavior was that the absolute maximum contrast would have occurred for an FRFT order $\kappa = 1$ when the chirp rate of the matched filter matched that of the signal. Since the maximum value occurred for $\kappa \neq 1$, additional testing is necessary to verify the possibility of an isolated result. We need to test whether applying a matched filter and using the extra degree of freedom provided by the FRFT [2] will allow the contrast to be maximized beyond that of FT matched filtering.

7.2.2 Enhanced Fractional Focusing (EFrF) using the CSA

The excellent results obtained and presented in Figures 6.15 and 6.16 suggest that the initial focusing of the CSA was not optimal; however, the only difference between the presented results was the value of the FRFT transform order. The CSA was produced within the same program without the application or the range and azimuth FRFT updates, indicating the optimal FRFT transform not only enhanced the PSLR but also improved the resolution or IRW. Although the FRFT optimization was applied in both the range and azimuth directions, the range or fast-time application provided an overall better enhance-

ment. Applying the FRFT before the first azimuth FFT and getting significant results, suggests that motion compensation may not have been optimal for this scene.

7.3 Future Research

7.3.1 LFM detection using the Discrete Chirp-Fourier Transform

As noted in Chapter 6, the mapping of the continuous FRFT to a discrete implementation requires significant up-sampling or interpolation, thus increasing the processing time. Although its implementation is $O(N\log_2 N)$ where N is the number of samples, its performance is considerably slower. A possible faster implementation for LFM detection is the use of the *discrete chirp-Fourier transform* (DCFT) which uses the DFT to match multiple chirps to multiple chirp components [46]. The definition of the DFT,

$$X(k) = \frac{1}{\sqrt{N}} \sum_{n=0}^{N-1} x(n) W_N^{nk}, \qquad 0 \le k \le N-1 \tag{7.2}$$

where $W_N = \exp(^{-j2\pi}/_N)$, the DCFT is

$$X_c(k,l) = \frac{1}{\sqrt{N}} \sum_{n=0}^{N-1} x(n) W_N^{ln^2+kn}, \qquad 0 \le k,l \le N-1 \tag{7.3}$$

where k represents the constant frequencies and l the chirp rates. The author indicates a relationship between the DCFT and FRFT exists in that the chirp rate parameter l is related to the rotational parameter of the FRFT. Note, this method does not have a relationship with the ambiguity function similar to FrACF, meaning a 2-D search is necessary to identify both k and l. It may be possible to minimize the 2-D search by constraining k and l to their expected values and some initial testing needs to be done to understand the performance.

7.3.2 Multi-component LFM Rate Resolution

While researching LFM detection using the FRFT, a question that was not answered deals with the resolution of the sweep rate parameter used to create the detection statistic

in FrACF. The idea being, if we understood a bound on the LFM rate resolution, that would provide a bound for the sweep rate resolution. The workaround for not having this bound, was to understand the LFM rate accuracy needed to minimize QPE. We were able to locate a recent work [37] where it is noted that there are no comparative works.

Based on the relationship of the FRFT with the WD, we tried locating a more generalized definition for chirp-rate resolution and time-frequency. As noted by Wang [35], resolution defined as the ability to separate two chirp signals with very small difference in chirp rate, has not been well defined.

Additional research is needed to identify additional work in the area of chirp rate resolution and the FRFT, or a more generalized definition for time-frequency.

7.3.3 LFM detection and instantaneous frequency

Since we used the signal SNR in our analysis, it should be noted that the multiplicative noise ratio (MNR) is a common image quality metric used for speckle imagery. The MNR is defined as the ratio of the image intensity in the no return area (NRA) divided by the intensity in a bright surrounding area [3]. There is work [44] indicating that the instantaneous frequency (IF) time-frequency estimation will be impacted by multiplicative noise and not possible for MNR > 1.0.

Additional research is needed using the signal model in [44] in place of the model provided with Equation (4.8) to understand the LFM detection performance for SAR LFM signals.

7.3.4 Matched filtering and time-bandwidth product

With the FRFT additivity of rotations property, it is possible to rotate the time-frequency (TF) plane of a chirp, throughout a continuous range of fractional domains or angles using

the rotational parameter α as depicted in Figure 3.3.

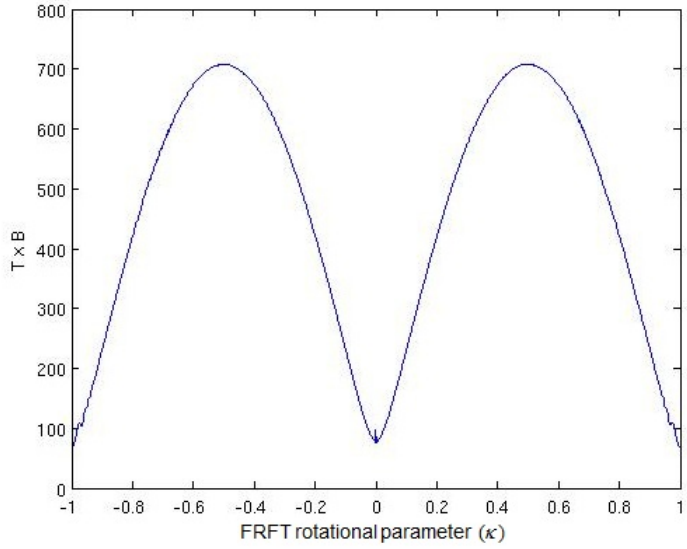

Figure 7.1: Chirp: time-bandwidth product for $-1 \leq \kappa \leq 1$.

Figure 7.1 is a plot of a RADARSAT-1 chirp rotated throughout the range of the FRFT using the additivity of rotations property and as expected, the time-bandwidth product (TBP) is maximized for $\alpha = \pm\pi/4$, where $\alpha = \kappa\pi/2$. Since the matched filtering process will cancel the rotation by applying a conjugate chirp, a study should be done to understand the results of applying the filter at the maximum TBP. As indicated in [42] the matched filter compression gain is attributed to the TBP and by Equation (4.19), we know that oversampling or zero padding the arrays used in pulse compression will cause a clockwise rotation in the TF plane decreasing the TBP. By use of the FRFT rotational parameter, it may be possible to enhance the compression gain by rotating both the matched filter and the signal to the maximum TBP.

7.3.5 Time-frequency methods for moving target and inverse synthetic aperture radar (ISAR) processing

The direct relationship of the FRFT to linear canonical transforms makes the FRFT an attractive transform for many TF applications. The focus of the work in this research was to estimate uncompensated motion and enhance the CSA processing by correcting the LFM chirp rates of stationary targets. If we were interested in processing the moving target information, then there is recent work using the FRFT for this purpose with many proposed methods [7, 8, 18, 36, 38]. As we demonstrated with the enhanced FRFT focusing (EFrF) technique using the CSA and RADARSAT-1 data, the implementation and characteristics of the data determined how the FRFT was used. We suspect there will be similar challenges in applying the FRFT to real data used for both moving target detection and inverse synthetic aperture radar (ISAR) processing. If real data is available, this work could be extended into these areas.

REFERENCES

[1] I. Cumming and F. Wong, *digital processing of Synthetic Aperture Radar Data*. Norwood, MA: Artech House, 2005.

[2] A. S. Amein and J. J. Soraghan, "A new chirp scaling algorithm based on the fractional Fourier transform," *IEEE Signal Processing Letters*, vol. 12, pp. 705–708, October 2005.

[3] R. J. Sullivan, *Microwave Radar: Imaging and Advanced Concepts*. Norwood, MA: Artech House, 2000.

[4] D. Munson and R. Visentin, "A signal processing view of strip-mapping synthetic aperture radar," *IEEE Transactions on Acoustics, Speech, and Signal Processing*, vol. 37, pp. 2131–2147, December 1989.

[5] J. Curlander and R. McDonough, *Synthetic Aperture Radar: Systems and Signal Processing*. New York, NY: Wiley, 1991.

[6] W. Carrara, R. Goodman, and R. M. Majewski, *Spotlight Synthetic Aperture Radar: Signal Processing Algorithms*. Artech House, 1995.

[7] V. Chen and H. Ling, *Time-Frequency Transforms for Radar Imaging and Signal Analysis*. Norwood, MA: Artech House, 2002.

[8] L. Du and G. Su, "Adaptive inverse synthetic aperture radar imaging for nonuniformly moving targets," *IEEE Geoscience and Remote Sensing Letters*, vol. 2, pp. 247–249, July 2005.

[9] J. Kolman, "Aperture weighting for maximum contrast of SAR imagery," *2008 IEEE Radar Conference*, pp. 1–6, May 2008.

[10] R. Raney, H. Runge, R. Balmer, I. Cumming, and F. H. Wong, "Precision SAR processing using chirp scaling," *IEEE Transactions on Geoscience and Remote Sensing*, vol. 32, pp. 786–799, July 1994.

[11] R. Namias, "The fractional order Fourier transform and its application to quantum mechanics," *Journal of the Institute of Mathematics and Its Applications*, vol. 25, pp. 241–265, April 1980.

[12] L. B. Almeida, "The fractional Fourier transform and time-frequency representations," *IEEE Transactions on Signal Processing*, vol. 42, pp. 3084–3091, November 1994.

[13] O. Akay and G. F. Boudreaux-Bartels, "Fractional convolution and correlation via operator methods and application to detection of linear FM signals," *IEEE Transactions on Signal Processing*, vol. 49, pp. 979–993, May 2001.

[14] O. Akay and G. F. Boudreaux-Bartels, "New fractional operators and their properties: A generalization of time and frequency operators," *IEEE 2nd UK Symposium on Applications of Time-Frequency and Time-Scale Methods*, pp. 141–144, August 1997.

[15] O. Akay and G. F. Boudreaux-Bartels, "Unitary and Hermitian fractional operators and their relation to the fractional Fourier transform," *IEEE Signal Processing Letters*, vol. 5, pp. 312–314, November 1998.

[16] O. Akay and G. Boudreaux-Bartels, "Fractional autocorrelation and its application to detection and estimation of linear FM signals," *Proceedings of the IEEE-SP International Symposium on Time-Frequency and Time-Scale Analysis*, pp. 213–216, 1998.

[17] O. Akay and E. Erözden, "Employing fractional autocorrelation for fast detection and sweep rate estimation of pulse compression radar waveforms," in *Signal Processing*, vol. 89, pp. 2479–2489, Elsevier, December 2009.

[18] H.-B. Sun, "Application of the fractional Fourier transform to moving target detection in airborne SAR," *IEEE Transactions on Aerospace and Electronic Systems*, vol. 38, pp. 1416–1424, October 2002.

[19] A. Papoulis, *Systems and Transforms with Applications in Optics*. New York: MaGraw-Hill, 1968.

[20] F. Hlawatsch and G. Boudreaux-Bartels, "Linear and quadratic time-frequency signal representations," *IEEE Signal Processing Magazine*, vol. 9, pp. 21–67, April 1992.

[21] R. Raney, "A new and fundamental Fourier transform pair," *International Geoscience and Remote Sensing Symposium*, pp. 106–107, May 1992.

[22] A. Amein and J. Soraghan, "Azimuth fractional transformation of the fractional chirp scaling algorithm (FrCSA)," *IEEE Transactions on Geoscience and Remote Sensing*, vol. 44, pp. 2871–2879, October 2006.

[23] H. M. Ozaktas, Z. Zalevsky, and M. A. Kutay, *The Fractional Fourier Transform: With Applications in Optics and Signal Processing*. Chicester, U.K.: Wiley, 2001.

[24] H. Ozaktas, N. Erkaya, and M. Kutay, "Effect of fractional Fourier transformation on time-frequency distributions belonging to the Cohen class," *IEEE Signal Processing Letters*, vol. 3, pp. 40–41, February 1996.

[25] H. M. Ozaktas, O. Arikan, M. A. Kutay, and G. Bozdagi, "Digital computation of the fractional Fourier transform," *IEEE Transactions on Signal Processing*, vol. 44, pp. 2141–2150, September 1996.

[26] A. Bultheel and H. M. Sulbaran, "Computation of the fractional Fourier transform," *Applied and Computational Harmonic Analysis*, vol. 16, no. 3, pp. 182–202, 2004.

[27] C. Candan, M. A. Kutay, and H. M. Ozaktas, "The discrete fractional Fourier transform," *IEEE Transactions on Signal Processing*, vol. 48, pp. 1329–1337, May 2000.

[28] A. Oppenheim and R. Schafer, *Digital Signal Processing*. Prentice Hall, 1975.

[29] A. Amein and J. Soraghan, "Fractional chirp scaling algorithm: Mathematical model," *IEEE Transactions on Signal Processing*, vol. 55, pp. 4162–4172, August 2007.

[30] P. Djurić and S. Kay, "Parameter estimation of chirp signals," *IEEE Transactions on Acoustics, Speech, and Signal Processing*, vol. 38, pp. 2118–2126, December 1990.

[31] S. Kay, *Fundamentals of Statistical Signal Processing:Detection Theory*. Upper Saddle River, NJ: Prentice-Hall, 1998.

[32] J. Mathews, *Numerical Methods for Computer Science, Engineering, and Mathematics*. Englewood Cliffs, NJ: Prentice-Hall, 1987.

[33] M. Wang, A. Chan, and C. Chui, "Linear frequency-modulated signal detection using Radon-ambiguity transform," *IEEE Transactions on Signal Processing*, vol. 46, pp. 571–586, March 1998.

[34] C. Capus and K. Brown, "Short-time fractional Fourier methods for the time-frequency representation of chirp signals," *Journal of the Acoustical Society of America*, vol. 113, pp. 3253–3263, June 2003.

[35] M. Wang, A. Chan, and C. Chui, "Wigner-Ville distribution decomposition via wavelet packet transform," *Proceedings of the IEEE-SP International Symposium on Time-Frequency and Time-Scale Analysis*, pp. 413–416, June 1996.

[36] X. Chen and J. Guan, "A fast FRFT based detection algorithm of multiple moving targets in sea clutter," *Proceedings IEEE International Radar Conference*, pp. 402–406, May 2010.

[37] L. Feng, H. Yu, T. Rao, and W. Yue, "Resolution ability of fractional Fourier transform in multi-component LFM signal chirp-rate," *4th International Conference on Wireless Communications, Networking and Mobile Computing (WiCOM)*, pp. 1–4, October 2008.

[38] C. Min, F. Yaowen, J. Weidong, L. Xiang, and Z. Zhaowen, "High resolution range profile imaging of high speed moving targets based on fractional Fourier transform," *Proceedings of the SPIE - The International Society for Optical Engineering*, vol. 6786, pp. 678654–1–9, November 2007.

[39] H. Li, B. Yu, W. Xi, and K. Wang, "A fractional Fourier approach SAR imaging method," *Congress on Image and Signal Processing*, vol. 5, pp. 215–218, May 2008.

[40] D. Sazbon, Z. Zalevsky, E. Rivlin, and D. Mendlovic, "Using Fourier/Mellin-based correlators and their fractional versions in navigation task," in *Journal of Pattern Recognition Society*, vol. 35, pp. 2993–2999, New York: Elsevier, 2002.

[41] S. Parashar, E. Langham, J. McNally, and S. Ahmed, "RADARSAT mission requirements and concept," *Canadian Journal of Remote Sensing*, vol. 19, pp. 280–288, November 1993.

[42] A. Mahmood, "RADARSAT-1 background mission monitoring of the arctic," *IEEE International Geoscience and Remote Sensing Symposium*, p. 4, July 2005.

[43] A. Doerry, "Performance limits for synthetic aperture radar - second addition," *Sandia Report SAND2006-0821*, p. 70, 2006.

[44] B. Barkat and B. Boashash, "IF estimation of linear FM signals corrupted by multiplicative and additive noise: A time-frequency approach," *IEEE International Con-*

ference on Acoustics, Speech, and Signal Processing, vol. 2, pp. 661–664, June 2000.

[45] J. Lee, K. Hoppel, and S. Mango, "Unsupervised estimation of speckel noise in radar images," *International Journal of Imaging Systems and Technology*, vol. 4, pp. 298–305, August 1992.

[46] X. Xia, "Discrete chirp-Fourier transform and its application to chirp rate estimation," *IEEE Transactions on Signal Processing*, vol. 48, pp. 3122–3133, November 2000.